Received: 13 May 2023 | Revised: 6 November 2023 | Accepted: 7 November 2023

DOI: 10.1111/jmg.12754

ORIGINAL ARTICLE

Journal of METAMORPHIC GEOLOGY WILEY

The inhibited response of accessory minerals during high-temperature reworking

Samantha March[1] | **Martin Hand**[1] | **Laura Morrissey**[1,2] | **David Kelsey**[3]

[1]Department of Earth Sciences, The University of Adelaide, Adelaide, South Australia, Australia

[2]Future Industries Institute, University of South Australia, Mawson Lakes, South Australia, Australia

[3]Geological Survey of Western Australia, East Perth, Western Australia, Australia

Correspondence
Samantha March, Department of Earth Sciences, The University of Adelaide, Adelaide, South Australia, Australia.
Email: samantha.march@adelaide.edu.au

Funding information
Australian Institute of Geoscientists; Australian Research Council, Grant/Award Number: DP220103037; Geological Society of Australia; Playford Trust; University of Adelaide; Robert Francis Thyer Award, Playford Trust PhD Scholarship; Australian Institute of Geoscientists Student Bursary; Geological Society of Australia Endowment Fund; Australian Research Council DECRA Fellowship, Grant/Award Number: DE210101126

Handling Editor: Prof. Richard White

Abstract

U–Pb zircon and monazite geochronology are considered to be among the most efficient and reliable methods for constraining the timing of high-temperature (*HT*) metamorphic events. However, the reliability of these chronometers is coupled to their ability to participate in reactions. A case study examining the responsiveness of zircon and monazite has been conducted using granulite facies metapelitic and metamafic lithologies in the Warumpi Province, central Australia. In some instances, metapelitic granulites from this locality are polymetamorphic, with an early M1 assemblage containing orthopyroxene, cordierite, biotite, quartz, ilmenite and magnetite, and an M2 assemblage represented by garnet, sillimanite, orthopyroxene, cordierite, biotite, sapphirine, ilmenite and magnetite. M2 metamorphism is linked to *HT* peak conditions of 8–10 kbar and 850–915°C. Detrital and metamorphic zircon and monazite from these rocks dominantly record U–Pb dates of 1670–1610 Ma and have trace element compositions suggesting they grew prior to peak M2 garnet in the rock. Lu–Hf geochronology from M2 garnet gives ages of c. 1150 Ma. Zircon and monazite are therefore suggested to have remained largely inert during *HT* metamorphism. We attribute the relatively minor response of zircon and monazite during high-temperature Mesoproterozoic metamorphism to the localized development of refractory bulk compositions at c. 1630 Ma during M1 metamorphism. This created refractory Mg–Al-rich bulk compositions that were unable to undergo significant partial melting, despite experiencing subsequent temperatures of ~900°C at c. 1150 Ma. In contrast, metapelitic and metamafic rocks in the area that did not develop refractory bulk compositions during M1 metamorphism were able to partially melt and record c. 1150 Ma accessory mineral U–Pb ages. These results contribute to a small, but growing number of case studies investigating the systematics of the U–Pb system in zircon and monazite in polymetamorphic *HT* terranes and their apparent resistance to isotopic resetting. Where disequilibrium is apparent, garnet Lu–Hf geochronology can form an important tool to interrogate the significance of accessory U–Pb ages. In the Warumpi Province in central Australia, c. 1640 Ma zircon U–Pb ages had previously been

interpreted to reflect the formation of *HT* garnet-bearing granulites during a collisional event. Instead, the garnet-bearing assemblages formed at c. 1150 Ma during the Mesoproterozoic, calling into question the existence of a late Palaeoproterozoic collisional system in central Australia.

KEYWORDS
HT metamorphism, metapelite, *P–T* pseudosection, U–Pb geochronology, Warumpi Province

1 | INTRODUCTION

Obtaining age constraints for mineral assemblages in high-grade polymetamorphic terranes often relies on U–Pb geochronology from accessory minerals such as zircon and monazite, in combination with detailed metamorphic petrology and corresponding pressure–temperature (*P–T*) calculations. The significance of these interpretations is dependent on the coupling of the former with the latter.

Zircon and monazite are highly relied on for U–Pb geochronology in high and ultrahigh-temperature (*HT*, *UHT*) terranes, due to having closure temperatures that are commonly interpreted to exceed 900°C (Cherniak et al., 2004; Cherniak & Watson, 2001; Lee et al., 1997). Growth of zircon and monazite requires system or local saturation in zirconium, phosphates and rare earth elements (REEs), and in *HT* rocks generally occurs as melt crystallizes (Fraser et al., 1997; Rubatto et al., 2001; Kelsey et al., 2008; Kelsey & Powell, 2010; Yakymchuk & Brown, 2014; T. E. Johnson et al., 2015). In *HT* terranes where melting does take place, U–Pb geochronology of monazite and zircon can therefore provide meaningful constraints for the timing and rate of tectono-metamorphic processes (e.g., Asami et al., 2002; Cutts et al., 2011; Korhonen et al., 2013; Sajeev et al., 2010; Santosh et al., 2006; Schmitz & Bowring, 2003; Xu et al., 2019).

However, in polymetamorphic terrains, first cycle metamorphism can reduce the potential for partial melting during subsequent events (e.g., Korhonen et al., 2012; Phillips et al., 2007; Tenczer et al., 2006; White & Powell, 2002; Yakymchuk & Brown, 2014). Consequently, even at (*U*)*HT* granulite facies conditions, later metamorphism has the potential to occur below the solidus. Indeed, previously dehydrated crust becomes more susceptible to *HT* metamorphism due to an inhibited endothermic ability to melt and the resultant redistribution of energy as heat (e.g., Brown & Korhonen, 2009; Clark et al., 2011; Morrissey et al., 2014; Schorn et al., 2018; Stüwe, 1995; Vielzeuf et al., 1990; Walsh et al., 2015). Importantly, this means that accessory minerals such as zircon and monazite—which are typically responsive in melt-bearing systems—can remain relatively resistant to updating their geochronologic record even during *HT-UHT* reworking (e.g., Diener et al., 2008; Korhonen et al., 2012; Morrissey et al., 2016; Vielzeuf et al., 1990; White & Powell, 2002). The direct ramification of this is the potential for accessory minerals to have only a minor record of major regional metamorphic events and to be largely decoupled from the bulk metamorphic mineral assemblage (Thiessen et al., 2019). *P–T* constraints derived from these mineral assemblages may therefore be incorrectly interpreted in terms of their age, leading to the formulation of tectonic models that may not be valid. Case studies, for example, Thiessen et al. (2019), are required in order to investigate the responsivity of accessory minerals in natural systems.

In this study we investigate granulite facies rocks from the Warumpi Province in central Australia. These rocks have previously been used to support a model for late Palaeoproterozoic (c. 1640 Ma) collision, leading to the formation of *HT-UHT* mineral assemblages (Scrimgeour, Kinny, et al., 2005). The region has also experienced Mesoproterozoic (c. 1150 Ma) reworking (Wong et al., 2015), resulting in a complex polymetamorphic history and creating potential interference between metamorphic assemblages and their associated accessory mineral U–Pb record.

We use U–Pb geochronology in zircon, monazite, and titanite, garnet Lu–Hf geochronology, zircon-garnet trace element partitioning and mineral equilibria forward modelling to interrogate polymetamorphic *HT* assemblages. Contrary to past interpretations and despite monazite and zircon dominantly recording c. 1630 Ma ages, results from this work show (*U*)*HT* metamorphism occurred at c. 1150 Ma rather than c. 1630 Ma. This study offers insight into the U–Pb system of accessory minerals in polymetamorphic terranes, highlighting that zircon and monazite can remain relatively inert even at (*U*)*HT* conditions.

2 | GEOLOGICAL BACKGROUND

The Warumpi Province (Figure 1) is located along the southern margin of the North Australian Craton (NAC) and records episodic magmatism, deformation and overprinting metamorphic events between 1640 and 1130 Ma

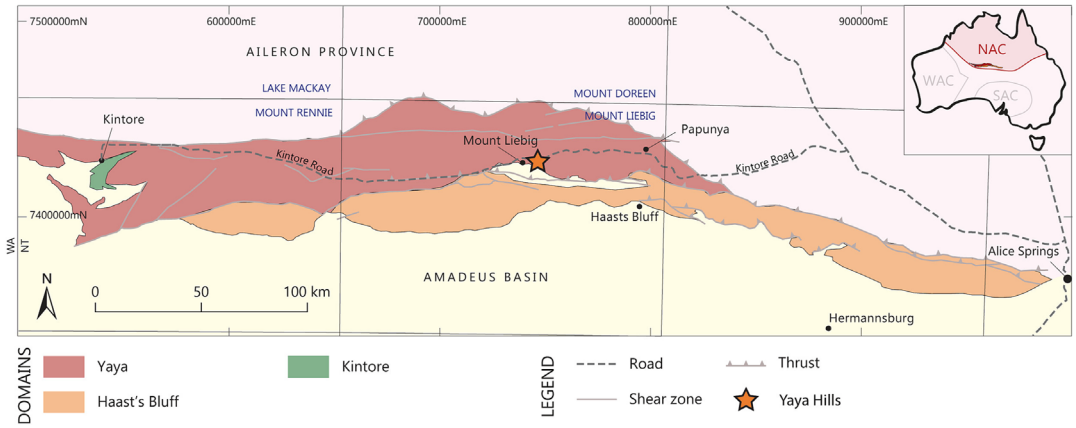

FIGURE 1 Simplified geological map of the Warumpi Province showing the Yaya, Haast's Bluff, and Kintore Domains. A star indicates the sampling location, Yaya Hills. Modified from the 1:2500k-scale map of the Northern Territory (Ahmad & Scrimgeour, 2006; Scrimgeour, 2013). Inset: a map of Australia showing the locations of the North, West and South Australian Cratons and the location of the Warumpi Province.

(Claoué-Long & Hoatson, 2005; Morrissey et al., 2011; Scrimgeour, Kinny, et al., 2005; Selway et al., 2006; Young et al., 1995). Based on differing protolith ages and metamorphic grade, the Warumpi Province can be divided into three fault-bound domains: the Yaya, Haasts Bluff and Kintore Domains. This study focuses on the Yaya Domain. The Yaya Domain occurs in the central and northern Warumpi Province, spanning ~300 km in length. It is characterized by granulite facies metamorphism in the east, which decreases to low- to medium-pressure upper amphibolite facies in the far west (Scrimgeour, Kinny, et al., 2005). The highest grades of metamorphism in the Yaya Domain occur in cordierite-rich metapelitic rock outcrops in the Yaya Hills.

Numerous events have affected the Warumpi Province (e.g., Ahmad & Munson, 2013), of which the c. 1640 Ma Liebig Orogeny and c. 1200–1100 Ma Musgrave Orogeny are the most notable. The 1640–1630 Ma Liebig Orogeny has previously been inferred to record the oblique accretion and suturing of the exotic Warumpi Province to the NAC (Close et al., 2005; Scrimgeour, Kinny, et al., 2005). Evidence used to support this interpretation included the rapid burial and exhumation of the Yaya Domain, and the preservation of a magmatic belt interpreted to be an arc (Scrimgeour, 2013; Scrimgeour, Kinny, et al., 2005). Previously, *(U)HT* metamorphism has been ascribed to the Liebig Orogeny, with conventional thermobarometry suggesting peak granulite facies conditions at 9–10 kbar and >800°C (Scrimgeour, Kinny, et al., 2005).

The Warumpi Province was structurally and thermally reworked at c. 1150–1130 Ma during the Musgrave Orogeny (Biermeier et al., 2003; Black & Shaw, 1995; Collins & Shaw, 1995; Morrissey et al., 2011; Scrimgeour, Kinny, et al., 2005; Wong et al., 2015). This event has been associated with magmatism, pervasive deformation, and high thermal gradient metamorphism at amphibolite to granulite facies conditions (Biermeier et al., 2003; Morrissey et al., 2011; Scrimgeour, Close, & Edgoose, 2005; Scrimgeour, Kinny, et al., 2005; Shaw et al., 1992; Wong et al., 2015).

2.1 | Study area

Samples described in this study come from the western Yaya Hills, previously named Hill 830, located ~200 km west of Alice Springs (Figure 1). They were collected in the vicinity of a kilometre-scale boudin consisting of weakly to unfoliated, Mg–Al-rich orthopyroxene-sillimanite-garnet granulite (Figure 3a–d), and sapphirine-, corundum- and kornerupine-bearing rocks that occur adjacent to metagabbro (Figure 2). In places, outcrops contain abundant, euhedral, cm-sized aggregates of sillimanite that are pseudomorphic after andalusite. Locally, thin layers of quartzite occur within the Mg-Al granulite and are interpreted represent relic bedding. Zircons give a range of ages between 1660 and 2500 Ma (Scrimgeour, Kinny, et al., 2005), which are interpreted to record detrital inputs into the sedimentary protolith. Zircons have narrow rims that give ages of c. 1640 Ma, which are interpreted to record *HT-UHT* metamorphism (Scrimgeour et al., 2005b). The boudin is enclosed by migmatitic felsic, mafic and metapelitic rocks (Figure 3e,f) that contrast with the non-migmatitic character of the boudin interior. Regionally, the migmatitic rocks are characterized by approximately east–west trending foliations, however in the vicinity of the boudin they are locally deflected. Kinematic indicators within the migmatitic rocks indicate top to the NE movement along shallow to moderate NE dipping fabrics. Wong et al. (2015) interpreted tectonic transport to have occurred during the c. 1150 Ma Musgrave Orogeny. U–Pb zircon ages

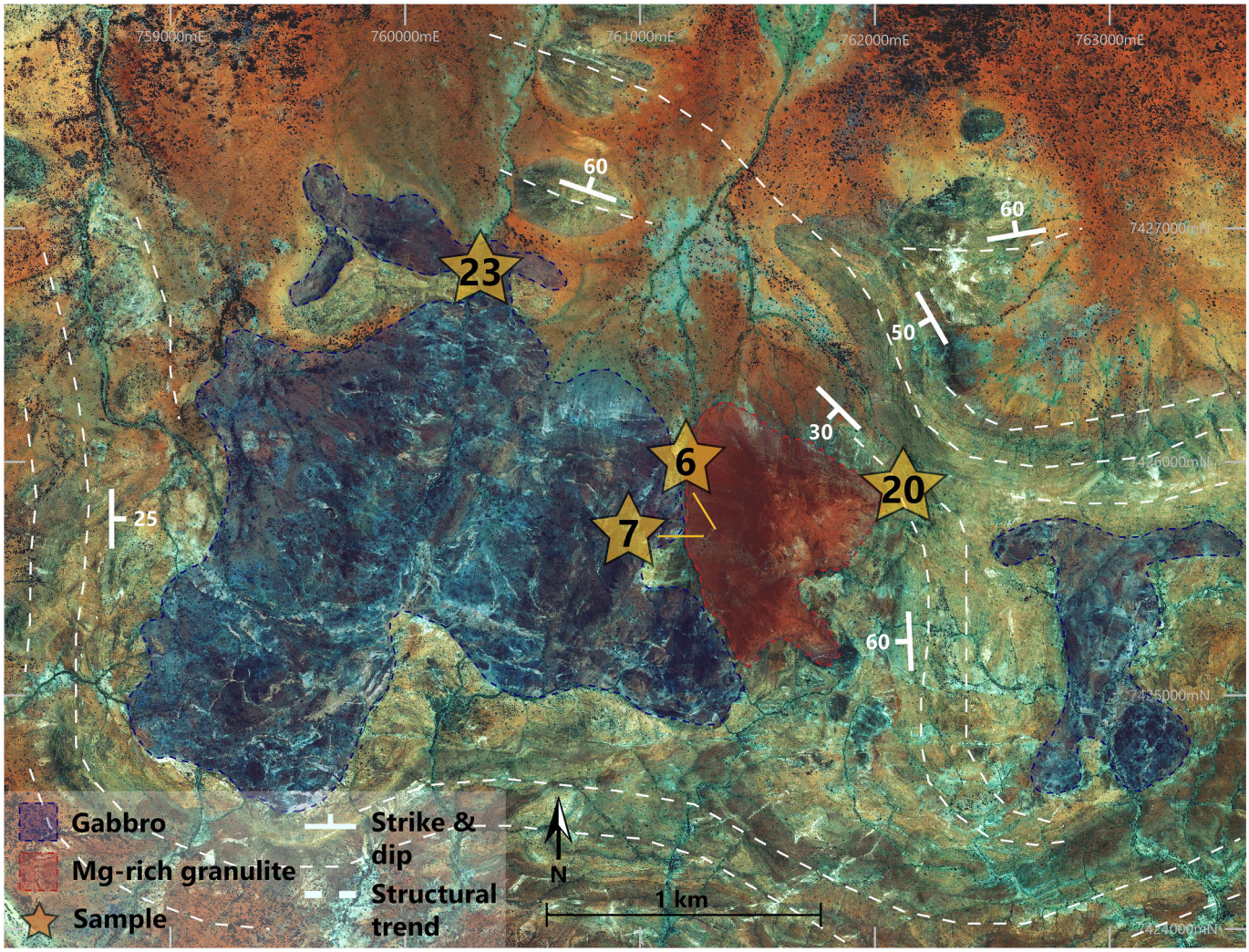

FIGURE 2 ESRI aerial image of the Yaya Hills and surrounds. The Yaya Hills are a granulite facies domain, indicated in red. Adjacent gabbro is coloured blue. Structural fabrics are indicated with dashed lines and annotated by strike and dip measurements. Sample locations are represented by orange stars.

from migmatitic felsic gneiss give two ages, one at c. 1570 Ma, and the other at c. 1150 Ma, both of which are interpreted to be metamorphic ages (Scrimgeour, Kinny, et al., 2005). Monazite from metapelitic samples give a range of ages consistent with growth at c. 1650–1610 Ma, and later modification at c. 1150 Ma (Wong et al., 2015).

3 | METHODS

3.1 | Whole-rock geochemistry

Whole-rock chemical compositional data required for the construction of mineral equilibria forward modelling were acquired at Bureau Veritas, Adelaide using 15–20 g of crushed material per sample. The geochemical aliquot for each sample was acquired from the thin section offcut in order to approximate a representative bulk composition as closely as possible. Sample material was fused with lithium metaborate and the fused glass digested in nitric acid. Subsequent inductively coupled plasma atomic emission spectroscopy (ICP-AES) and mass spectrometry (ICP-MS) analysis were used to measure major and trace elements, respectively. Geochemical data are presented in Table S1.

3.2 | Major element mineral compositions

Major element mineral compositions were acquired at Adelaide Microscopy, using a CAMECA SXFive Electron Probe Microanalyser (EPMA). The EPMA is equipped with five wavelength-dispersive spectrometers and uses PeakSite v6.4 software for microscope operation, along with Probe for EPMA software. Minerals were analysed

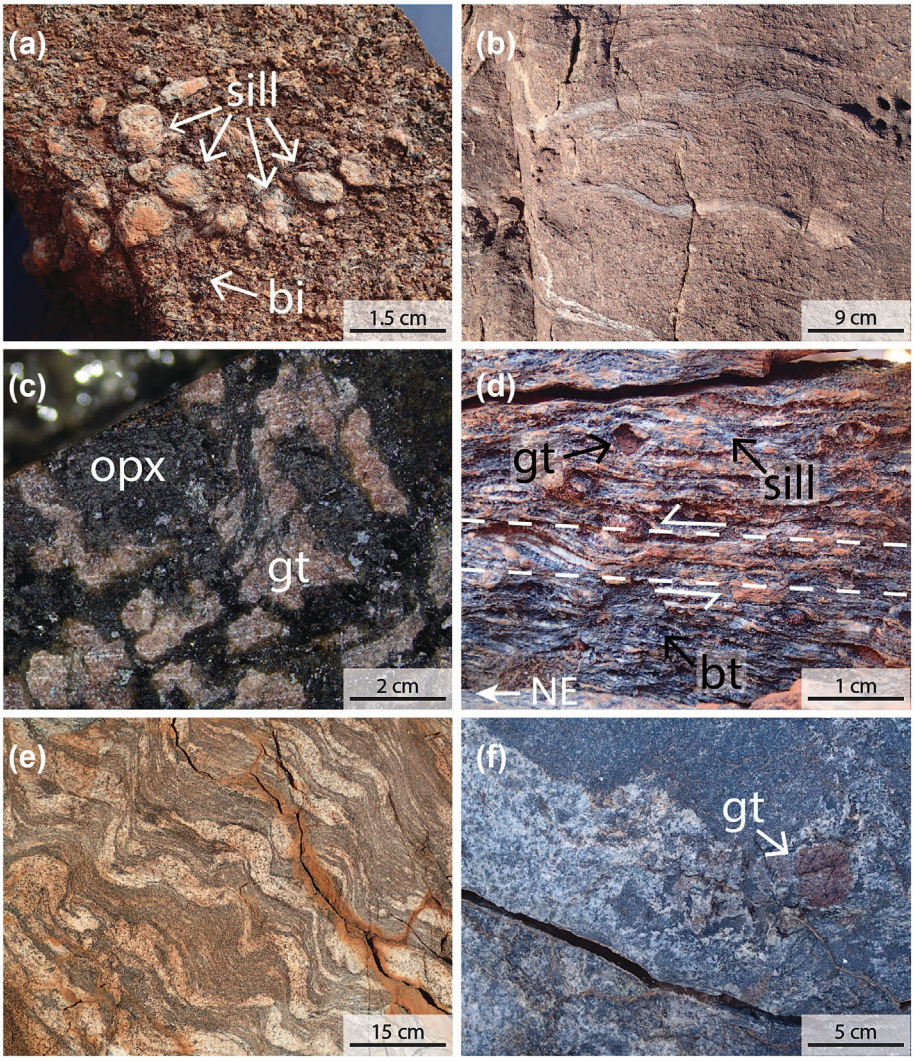

FIGURE 3 Field photographs from the Warumpi Province. (a) Metamorphic andalusite pseudomorphed by sillimanite in HT Mg-rich granulites. (b) Quartzite bedding in a HT Mg-rich orthopyroxene-garnet-sillimanite-cordierite metapelite. (c) M2 garnet coronas around M1 orthopyroxene in sample 830-7. (d) S-C fabric in garnet-sillimanite-biotite metapelitic gneiss with top to the NE (left) shear sense. (e) Migmatitic body from the sample 830-20 location. (f) Garnet-bearing leucosome hosted in sample 830-23 metamafic.

using a 20 nA beam current, 15 kV accelerating voltage, and a 5 μm spot size. Cl, Ca, K and Ba were analysed using the PET crystal; F on the PC0; Ti and P on the PET; Na, Si, Mg and Al on the TAP; and Fe, Mn, Cr and Ni on the LIF. The following reference materials were used: Cl—tugtupite, Ca—wollastonite, K—orthoclase, Ba—barite, F—MgF2, P—apatite, Ti—rutile, Na, Si—albite, Mg—olivine, Al, Fe—almandine garnet, Mn—rhodonite, Cr—chromium oxide and Ni—nickel olivine. Mineral formula stoichiometric charge balanced mineral recalculations were used to determine the amount of Fe^{3+} present in iron-bearing minerals (Droop, 1987). This was used to guide oxidation state for mineral equilibria forward modelling.

3.3 | Mineral equilibria forward modelling

Mineral equilibria models were calculated using GeoPS v3.2 software in the model system MnNCKFMASHTO ($MnO\text{-}Na_2O\text{-}CaO\text{-}K_2O\text{-}FeO\text{-}MgO\text{-}Al_2O_3\text{-}SiO_2\text{-}H_2O\text{-}TiO_2\text{-}O$) using the internally consistent thermodynamic dataset 'HP622' (Holland & Powell, 2011; Xiang & Connolly, 2021). Metapelitic activity-composition (*a–x*) models were used to calculate pseudosections for samples 830-6, 830-7 and 830-20 (Holland & Powell, 2003; Wheller & Powell, 2014; White et al., 2000, 2002, 2014), and metamafic *a-x* models for sample 830-23 (Green et al., 2016; Holland & Powell, 2003, 2011; Jennings & Holland, 2015; White et al., 2000, 2002, 2007, 2014).

Bulk compositions were determined combining mineral modal proportions derived from SEM mapping, and their compositions. This was done because the rocks are compositionally domanial. Simply using bulk rock geochemical analyses would homogenize compositional domain, creating non representative bulk compositions. Prior to constructing *P–T* models, pressure–oxidation state ($P–M_O$) and temperature–H_2O content ($T–M_{H2O}$) models were calculated to constrain the sensitivity of mineral assemblages to bulk oxidation state and water content, respectively (Appendix SA). Temperatures of 850°C and

pressures of 8 kbar were assigned in all models, excluding sample 830-20, based on previous *P–T* constraints for the sample location (Scrimgeour, Kinny, et al., 2005). $P–M_O$ calculations for sample 830-20 were performed using a temperature of 750°C, based on constraints from Zr-in-rutile thermometry (Table S2). Modal proportions of oxides and hydrous minerals were used in the interpretation of preliminary $T–M_{H2O}$ and $P–M_O$ diagrams.

3.4 | LA–ICP–MS: Geochronology and trace elements

3.4.1 | U–Pb geochronology

Monazite and zircon U–Pb isotopic data were collected using a RESOlution LR 193 nm excimer laser system at Adelaide Microscopy, Australia. Earlier sessions used a coupled Agilent 7700s inductively coupled plasma mass spectrometer (ICP–MS), and later sessions used an Agilent 8900 triple quadrupole ICP–MS (ICP–QQQ). Titanite U–Pb isotopic data was collected using the RESOlution LR 193 nm Excimer laser system coupled with the Agilent 8900 ICP–QQQ. Operating conditions are detailed in Table 1.

Monazite was analysed in-situ for samples 830-6, 830-7 and 830-20 and referenced to primary reference material, MAdel (518.4 ± 1 Ma; updated from Payne et al., 2008, with additional TIMS analysis), and in-house secondary reference materials, Ambat (~525 Ma) and 222 (450.2 ± 3.4 Ma; Maidment, 2005). BSE images were used to guide spot locations. Using the Agilent 7700s ICP–MS, samples 830-6 and 830-7 were analysed across two analytical sessions. Across those sessions, Ambat and 222 gave $^{206}Pb/^{238}U$ weighted mean ages of 518 ± 2 Ma ($n = 28$, MSWD = 0.8) and 450 ± 3 Ma ($n = 25$, MSWD = 2.3), respectively. Sample 830-20 was analysed using the Agilent 8900 ICP–QQQ. Secondary reference material 222 gave a $^{206}Pb/^{238}U$ weighted mean age of 456 ± 2 Ma ($n = 3$, MSWD = 0.68).

In situ analysis of titanite in sample 830-23 was calibrated against primary reference material, MKED (1517.0 ± 0.32 Ma; Spandler et al., 2016), and secondary reference material Mt Painter (442.6 ± 1.8 Ma; Elburg et al., 2003). Mt Painter gave a $^{206}Pb/^{238}U$ weighted mean age of 448.0 ± 3.0 Ma ($n = 10$, MSWD = 1.7).

Zircon grains were separated to be analysed in grain mounts using a SelFrag at John de Laeter Research Centre, Curtin University. Cathodoluminescence images were used to guide spot locations. Zircon U/Pb and Pb/Pb were calibrated against primary reference material GJ (608.5 ± 0.4 Ma; Jackson et al., 2004), with data accuracy monitored using secondary reference materials 91,500 (1065.4 ± 0.3 Ma; Wiedenbeck et al., 1995) and Plesovice (337.1 ± 0.4 Ma; Sláma et al., 2008). Zircons were analysed with a total acquisition time of 60 s, comprising 30 s of background measurement and 30 s of ablation. Using the Agilent 7700s ICP–MS across two analytical sessions, Plesovice and 91,500 yield $^{206}Pb/^{238}U$ and $^{207}Pb/^{206}Pb$ weighted mean ages of 339 ± 1 Ma ($n = 60$,

TABLE 1 LA–ICP–MS operating conditions.

Mineral	Sample/ analysis type	ICP-MS	Spot size (μm)	Fluence (J/cm^2)	Energy (mJ)	Frequency (Hz)
Zircon U–Pb and trace elements	830-7	Agilent 7700s	20	1.92	50	5
	830-6, 830-23	Agilent 7700s	30	1.92	50	5
	830-20	Agilent 8900	30	2	65	5
Monazite U–Pb and trace elements	830-6, 830-7	Agilent 7700s	13	1.51	45	5
	830-6, 830-7	Agilent 7700s	13	1.77	50	5
	830-20	Agilent 8900	30	2	65	5
Titanite U–Pb and trace elements	830-23	Agilent 8900	67	3.5	45	5
Garnet trace elements	830-6, 830-7	Agilent 7700s	30	2.84	33	5
	830-23	Agilent 8900	60	9	60	5
	830-20	Agilent 8900	60	9	60	5
Garnet Lu–Hf	830-20	Agilent 8900	257/173	3.62	45	10
	830-6	Agilent 8900	120	3.63	43	10
	830-6	Agilent 8900	257/173	2.32	70	10

MSWD = 2.1) and 1064 ± 15 Ma (n = 60, MSWD = 1), respectively in the first session. Using the Agilent 8900 ICP–QQQ, the second analytical session yields a Plesovice $^{206}Pb/^{238}U$ weighted mean age of 336 ± 2 Ma (n = 8, MSWD = 0.1) and 91,500 yields a $^{207}Pb/^{206}Pb$ age of 1049 ± 23 Ma (n = 8, MSWD = 1.6).

Data processing and reduction for all U–Pb geochronology was performed using Iolite 3.6 software (Hellstrom et al., 2008; Paton et al., 2011). Concordia plots were generated using IsoplotR (Vermeesch, 2018). Only concordant analyses were used in the calculation of sample weighted mean dates, where concordance is defined as being within 2σ uncertainty of concordia. Discordant analyses are shown as unfilled ellipses where they fall within the window of the concordia plot. Isotopic data and trace element concentrations, along with extended morphological and zoning descriptions for relevant minerals are given in Appendices S2–S6.

3.5 | Trace elements

Trace element data were acquired for monazite, zircon, titanite and garnet using a RESOlution LR 193-nm excimer laser system at Adelaide Microscopy, Australia (Tables S3–S6). Operating conditions are detailed in Table 1. Iolite 3.6 software (Hellstrom et al., 2008; Paton et al., 2011) was used for data processing and reduction, with synthetic glass, NIST610, monitored to confirm data reduction accuracy (Pearce et al., 2007). Ce was used as the internal standard for monazite (index content = 20.00 wt%), Zr for zircon (index content = 43.14 wt%), Ti for titanite (index content = 18.16 wt%) and Al for garnet (index content = 12.10 wt%). Monazite, zircon and titanite trace elements were collected at the same time as U–Pb geochronology. Zircon-garnet trace element ratios were calculated for Paleoproterozoic- and Mesoproterozoic-aged zircon relative to representative averages of garnet core and garnet rim analyses. The envelopes on these figures represent the full compositional range for zircon in each age population. Representative garnet core and garnet rim averages were determined by looking for marked and consistent changes in composition across traverses. There is ambiguity in this approach, increased by garnet in sample 830-6 and 830-7 being coronitic and not abiding by classic core to rim growth.

3.6 | Lu–Hf garnet geochronology

Lu–Hf isotopic data were collected across three analytical sessions from polished garnet rock blocks using a RESOlution 193-nm excimer laser ablation system coupled to an Agilent 8900 ICP–QQQ at Adelaide Microscopy, Australia (Table S7). Methods followed are those detailed in Simpson et al. (2021) and operating conditions are given in Table 1. Analysis involved 30 s of background, 40 s of ablation, and 30 s of washout time. NIST610 glass was used as the primary reference material and has a $^{176}Lu/^{177}Hf$ ratio of 0.1379 ± 0.005 and a $^{176}Hf/^{177}Hf$ ratio of 0.282111 ± 0.000009 (Nebel et al., 2009). Garnet from the Högsbo pegmatite and Black Point were used as secondary reference materials, where Högsbo was used to correct and propagate any age offset related to static fractionation by multiplying measured $^{176}Lu/^{176}Hf$ values for unknowns by the measured Högsbo age divided by the known Högsbo age. The columbite U–Pb age of the Högsbo pegmatite is 1029 ± 1.7 Ma (Romer & Smeds, 1996; Simpson et al., 2021), and monazite from Black Point gives a U–Pb age of c. 1743 Ma (in-house). Sample 830-20 was analysed in the first analytical session, where Högsbo gives an isochron age of 1077 ± 9 Ma (n = 15, MSWD = 0.94). Applying a correction to accommodate for the age offset in Högsbo, Black Point yields an isochron age of 1746 ± 23 Ma (n = 20, MSWD = 1.4). 830-6 was analysed across two sessions. In the first, Högsbo yields an isochron age of 1074 ± 13 Ma (n = 23, MSWD = 1.3), and Black Point a corrected isochron age of 1728 ± 19 Ma (n = 30, MSWD = 1.5). In the second analytical session, Högsbo gives an isochron age of 1072 ± 12 Ma (n = 18, MSWD = 1.6), and Black Point a corrected isochron age of 1737 ± 19 Ma (n = 30, MSWD = 1.7). The MSWD for Black Point in the second analytical session for sample 830-6 indicates a higher than expected degree of overdispersion.

Garnet Lu–Hf isotopic data processing and reduction was completed using the LADR software package (Norris & Danyushevsky, 2018). Ablation signals do not indicate that downhole fractionation is significant (Simpson et al., 2021). Lu–Hf isochron ages were calculated using IsoplotR (Vermeesch, 2018) and used a ^{176}Lu decay constant of 0.0001867 ± 0.00000008 Myr^{-1} (Scherer et al., 2001; Söderlund et al., 2004).

4 | RESULTS

4.1 | Petrography

4.1.1 | 830-6

This sample is weakly foliated and comes from within the low strain boudin domain shown in Figure 2. It contains orthopyroxene, garnet, biotite, sillimanite, cordierite, magnetite, plagioclase, and rare quartz, K-feldspar and spinel.

Texturally, there are two distinct mineral assemblages (Table 2). The first formed assemblage (M1) consists of coarse-grained orthopyroxene, cordierite, quartz, plagioclase and K-feldspar and is overprinted by coarse-grained biotite (Figure 4a). M1 orthopyroxene grains are coarse-grained (up to 4 by 1 mm), elongate, and distributed in a roughly layered arrangement that comprises ~40% of the rock (Figure 4a). These are interspersed with coarse-grained cordierite (up to 8 mm) that may be intergrown with quartz. Overall, M1 minerals comprise the bulk of the rock. The second-generation assemblage, designated M2, formed primarily via an adjustment in the mode of M1 cordierite. It includes fine-grained orthopyroxene, sillimanite, ilmenite, magnetite and biotite, all of which occur abundantly throughout M1 cordierite (Figure 4b,c). M2 orthopyroxene commonly forms coronas at the contact between cordierite and quartz (Figure 4b). In addition, M2 orthopyroxene often occurs as fine-grained rims around primary M1 orthopyroxene (Figure 4c). Garnet forms in clusters that comprise ~5% of the sample. Garnet contains abundant inclusions of sillimanite, together with biotite, cordierite and quartz, and may enclose M1 orthopyroxene (Figure 4d). This relationship suggests garnet forms part of the M2 assemblage. Where garnet occurs in close proximity to coarse-grained M1 cordierite, the orientation of inclusions in the garnet is reminiscent of the M2 minerals overgrowing cordierite, indicating garnet may be comparatively late in the M2 assemblage. Garnet is in contact with all minerals in the rock, including fine-grained cordierite, suggesting cordierite may also be an M2 mineral. A feature of the M2 assemblage is the common presence of extremely abundant, fine-grained (<5 μm) zircon and monazite grains (Appendix SB).

TABLE 2 Summary of M1 and M2 minerals in polymetamorphic samples 830-6 and 830-7.

	830-6		830-7	
Mineral	**M1**	**M2**	**M1**	**M2**
Orthopyroxene	√	√	√	√
Cordierite	√	√	√	√
Quartz	√		√	
Biotite	√	√	√	√
K-feldspar	√			√
Ilmenite		√	√	√
Magnetite		√	√	√
Garnet		√		√
Sillimanite		√		√
Sapphirine				√

4.1.2 | 830-7

This sample is unfoliated, and similar to sample 830-6, consists of two texturally distinct mineral assemblages (Table 2). The M1 assemblage comprises coarse-grained orthopyroxene (up to 3 by 1.5 mm), cordierite (~2 by 1 mm), biotite, quartz, ilmenite and magnetite. In places, this assemblage is well-preserved, but in other places has been extensively overprinted—and often completely obliterated—by M2 minerals. The M2 assemblage comprises garnet, sillimanite, orthopyroxene, cordierite, biotite, sapphirine, ilmenite and magnetite. At thin section scale, M2 garnet occurs as irregular-shaped porphyroblasts that locally rim M1 orthopyroxene (Figure 4e). However, within the hand sample it is evident M2 garnet forms large coronas around M1 orthopyroxene (Figure 3c). Garnet contains inclusions of cordierite, biotite, plagioclase, magnetite, ilmenite and fine-grained sillimanite. Although abundant in garnet, sillimanite inclusions are absent in M1 orthopyroxene suggesting it post-dates the M1 assemblage (Figure 4e). In areas of the rock where garnet is not present, M1 orthopyroxene forms an association with coarse-grained M1 cordierite and biotite. The M2 garnet is surrounded by a cordierite-rich matrix and commonly separated from M1 biotite by symplectitic cordierite, magnetite, and rare K-feldspar (Figure 4f). In other places, cordierite is associated with M2 orthopyroxene, which forms symplectites along the margins of garnet, and coronas around quartz and biotite (Figure 4g). The presence of orthopyroxene at the margins of garnet intergrown with cordierite suggests that the cordierite that surrounds the garnet is an M2 mineral that formed in association with M2 orthopyroxene. In contrast to the abundance of sillimanite inclusions in garnet, sillimanite is rare in M2 cordierite, indicating both garnet and sillimanite were consumed by M2 cordierite. Ilmenite, sapphirine, biotite and quartz also occur within M2 cordierite (Figure 4h). Sapphirine typically forms clusters of bladed grains within M2 cordierite, but rarely occurs in contact with garnet. Quartz exists throughout the rock but is less common within the M2 cordierite-rich domains. The interpreted petrological evolution recorded by the sample is a coarse-grained orthopyroxene-biotite-cordierite-quartz assemblage (M1), overprinted by an M2 assemblage containing sillimanite and garnet that once coexisted with M1. In the final stage, secondary M2 cordierite and orthopyroxene, along with sapphirine, ilmenite and magnetite, formed at the expense of M2 garnet. Similar to sample 830-6, the M2 assemblage volumes commonly contain abundant very fine-grained (<5 μm) zircon and monazite (Appendix SB).

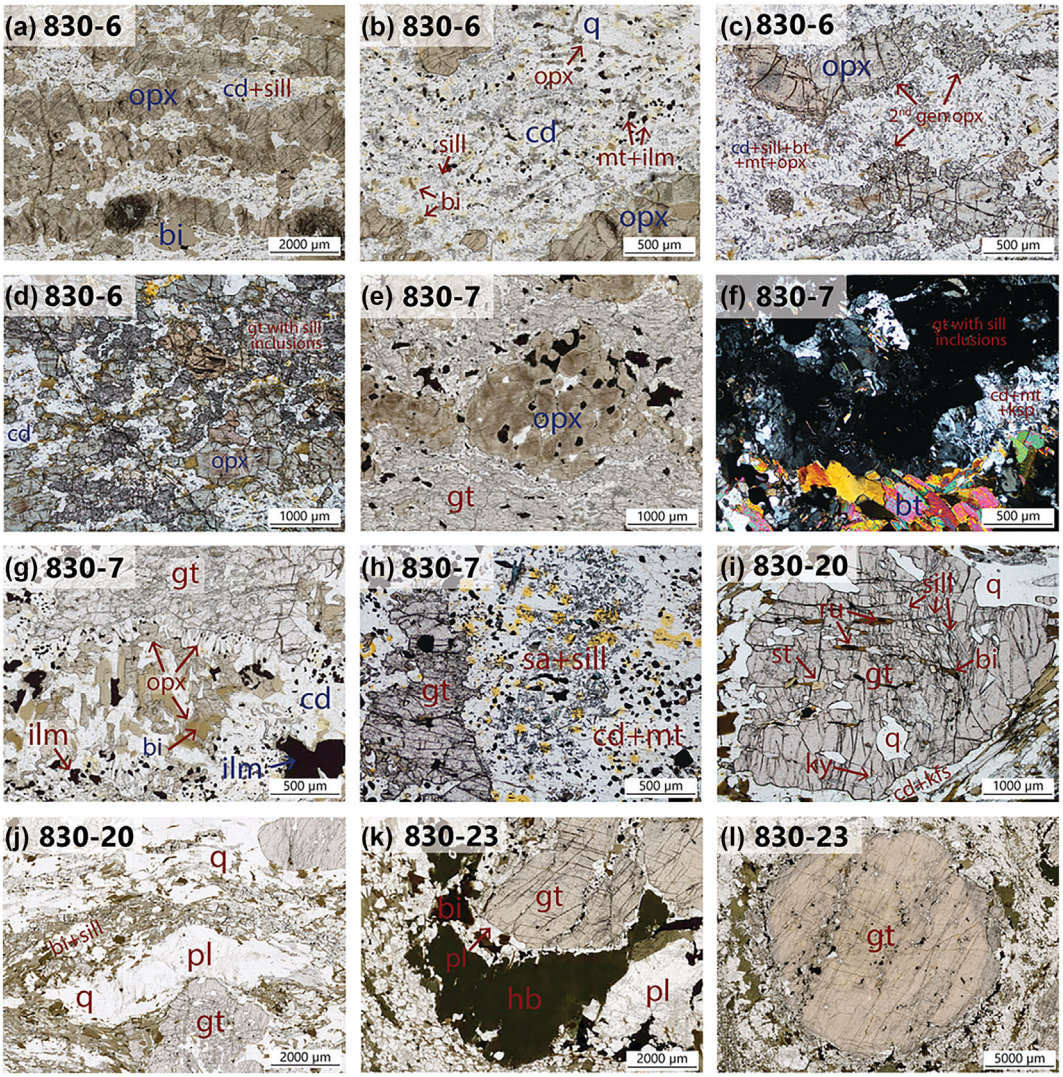

FIGURE 4 Photomicrographs from this study, where blue indicates M1 minerals and red indicates M2 minerals. (a) 830-6: Layered, coarse-grained orthopyroxene intergrown with coarse-grained cordierite. (b) 830-6: Fine-grained sillimanite, biotite, orthopyroxene, magnetite, and ilmenite, overgrowing coarse-grained cordierite. (c) 830-6: Orthopyroxene forming along the grain boundaries of orthopyroxene in a matrix of cordierite hosting sillimanite, biotite, magnetite, and orthopyroxene. (d) 830-6: Garnet with abundant sillimanite inclusions. Garnet occurs in close proximity to orthopyroxene. (e) 830-7: Garnet coronas around orthopyroxene. (f) 830-7: Cordierite-magnetite-K-feldspar symplectites separating biotite from garnet. (g) 830-7: Orthopyroxene-cordierite symplectites around garnet, and orthopyroxene coronas around biotite and ilmenite. (h) 830-7: A sapphirine-sillimanite-cordierite symplectite replacing garnet. (i) 830-20: Kyanite, sillimanite, staurolite, rutile, biotite and quartz inclusions inside porphyroblastic garnet. (j) 830-20: A quartz-plagioclase leucocratic lens parallel to the matrix foliation. (k) 830-23: A plagioclase corona separating garnet and hornblende. (l) 830-23: Coarse-grained, partially replaced garnet surrounded by an annulus of plagioclase-hornblende-biotite-K-feldspar-ilmenite-magnetite. Abbreviations: bi = biotite, cd = cordierite, gt = garnet, hb = hornblende, ilm = ilmenite, ky = kyanite, mt = magnetite, opx = orthopyroxene, pl = plagioclase, q = quartz, = ru = rutile, sa = sapphirine, sill = sillimanite.

4.1.3 | 830-20

Sample 830-20 is texturally less complex than samples 830-6 and 830-7. Sample 830-20 is strongly foliated and comes from the migmatitic domain that encloses the low strain boudin domain shown in Figure 2. Garnet grain size is bimodal, defined by a coarse-grained population (~6 mm) with inclusion-rich cores and inclusion-poor rims, and a finer-grained population (~1 mm) devoid of inclusions. The coarse-grained garnet cores contain abundant sillimanite that commonly occurs as polymineralic aggregates, and in some cases relic kyanite is also preserved. In addition to aluminosilicate inclusions, garnet contains quartz, staurolite, rutile, biotite, zircon, monazite and magnetite (Figure 4i). The matrix foliation is defined by sillimanite and biotite, with less abundant

quartz, plagioclase, and ilmenite. This foliation wraps porphyroblastic garnet and plagioclase-quartz lenses (Figure 4j). Quartz and prismatic sillimanite may contain inclusions of rutile and ilmenite. Prismatic sillimanite is rimmed by finer-grained sillimanite intergrown with biotite. The bulk of matrix biotite grows around the margins of sillimanite and is therefore interpreted to postdate the foliation-defining sillimanite. In places biotite and sillimanite are separated from garnet by cordierite and minor K-feldspar. Elsewhere, cordierite locally separates the foliation-defining sillimanite from biotite.

4.1.4 | 830-23

Sample 830-23 is proximal to the margin of the mafic body in Figure 2, where it is in contact with the regionally surrounding migmatitic rocks. The sample is foliated and contains porphyroblastic garnet (up to 3 cm) that occurs in deformed, coarse-grained, leucocratic segregations comprising plagioclase with minor hornblende and biotite. The leucocratic segregations are interpreted to represent the former presence of melt. Garnet contains rare inclusions of plagioclase and magnetite, and occasionally titanite. Surrounding the garnet-bearing leucocratic segregations are hornblende and biotite in a matrix dominated by plagioclase (Figure 4k), together with minor quartz, K-feldspar, ilmenite and magnetite. Rare titanite grains (up to ~1000 μm) also occur in the matrix. The interpreted peak metamorphic assemblage comprises garnet-plagioclase-hornblende-biotite-K-feldspar-ilmenite-magnetite-titanite and melt. At its margins, garnet has been replaced by an assemblage of plagioclase-hornblende-biotite-K-feldspar-ilmenite-magnetite, with some relic garnet also preserved (Figure 4l). Although with inherent uncertainties, the width of this reaction annulus allows the sizes of the original garnet grains to still be discerned, suggesting ~15% of the garnet has been replaced. The present garnet abundance is 8%, indicating the peak assemblage once had ~9.5% garnet.

4.2 | Mineral chemistry

Representative endmember compositions for garnet, orthopyroxene, biotite, plagioclase, hornblende, cordierite, ilmenite and magnetite are presented in Table 3, and respective cation calculations in Table 4.

4.2.1 | Garnet

Garnet compositions are similar in samples 830-6 and 830-7. Garnet is dominantly almandine, with X_{alm} (Fe^{2+}/[Fe^{2+} + Ca + Mg + Mn]) values of 0.47–0.52 in the cores increasing to values of 0.49–0.56 in the rims. X_{grs} (Ca/[Fe^{2+} + Ca + Mg + Mn]) and X_{sps} (Mn/[Fe^{2+} + Ca + Mg + Mn]) are unzoned. X_{py} (Mg/[Fe^{2+} + Ca + Mg + Mn]) shows rimward depletion with values decreasing from 0.40–0.45 to 0.33–0.42 in sample 830-6, and 0.41–0.42 to 0.39–0.42 in sample 830-7. Garnet in sample 830-20 has X_{alm} values of 0.47–0.50 in the cores, increasing to 0.50–0.56 in the rims. Pyrope values (X_{py}) range from 0.40 to 0.45 in the cores to 0.33–0.43 in the rims. X_{grs} is unzoned and ranges from 0.04–0.06 and X_{sps} values are below 0.02. Garnet in sample 830-23 has X_{alm} values of 0.52–0.57 in the core and 0.58–0.73 in the rim. X_{py} is <0.02–0.03 in cores and 0.07–0.17 in rims, X_{grs} is 0.20–0.24 in cores and comparatively depleted in rims (0.10–0.20), and X_{sps} values are 0.12–0.15 in the core, decreasing to <0.02–0.06 in the rim.

4.2.2 | Cordierite

Cordierite occurs in all metapelitic samples and shows little compositional variation within each sample. X_{Fe} (Fe^{2+}/[Fe^{2+} + Mg]) values are 0.05–0.09 in sample 830-6, 0.01–0.08 in sample 830-7, and 0.08–0.19 in sample 830-20.

4.2.3 | Orthopyroxene

M1 and M2 orthopyroxene is present in samples 830-6 and 830-7. M1 orthopyroxene in sample 830-6 records X_{Fe} (Fe^{2+}/[Fe^{2+} + Mg]) and Y_{opx} (x [Al,M1]) values of 0.27–0.31, and 0.08–0.13, respectively. M2 orthopyroxene has X_{Fe} values of 0.27–0.33 and Y_{opx} values of 0.10–0.16. Sample 830-7M1 orthopyroxene has X_{Fe} values of 0.24–0.30 and Y_{opx} values of 0.04–0.13. M2 orthopyroxene from sample 830-7 has X_{Fe} values of 0.27–0.31 and Y_{opx} values of 0.06–0.12. Al_2O_3 traverses across M1 orthopyroxene in samples 830-6 and 830-7 are given in Appendix SC.

4.2.4 | Biotite

X_{Fe} (Fe^{2+}/[Fe^{2+} + Mg]) values are consistent across metapelitic samples, ranging from 0.17 to 0.19. TiO_2 concentrations are lowest in sample 830-6, ranging from 1.17 to 1.29 wt%. In sample 830-7, TiO_2 concentrations are 1.30 to 1.39 wt%, and in 830-20 range from 1.22 to 1.85 wt%. Al_2O_3 concentrations also differ between samples, ranging from 7.87 to 8.36 wt% in 830-6, 8.27 to 8.68 wt% in 830-7, and 9.09 to 10.09 wt% in 830-20.

TABLE 3 Summary of mineral chemistry for samples 830-6, 830-7, 830-20 and 830-23.

Mineral	End-member proportions	830-6	830-7	830-20	830-23
Garnet core	X_{gt}	0.50–0.52	0.52–0.54	0.50–0.54	0.84–0.86
	X_{alm}	0.47–0.50	0.51–0.52	0.47–0.50	0.52–0.57
	X_{py}	0.40–0.45	0.41–0.42	0.40–0.45	<0.02–0.03
	X_{grs}	0.04–0.06	<0.02	0.04–0.06	0.20–0.24
	X_{sps}	<0.02	<0.02	<0.02	0.12–0.15
Garnet rim	X_{gt}	0.52–0.59	0.53–0.58	0.53–0.59	0.78–0.82
	X_{alm}	0.49–0.56	0.52–0.56	0.50–0.56	0.58–0.73
	X_{py}	0.33–0.42	0.39–0.42	0.33–0.43	0.07–0.17
	X_{grs}	0.04–0.06	<0.02	0.04–0.05	0.10–0.20
	X_{sps}	<0.02	<0.02	<0.02	<0.02–0.06
Orthopyroxene (M1)	X_{Fe}	0.27–0.31	0.24–0.30	–	–
	Y_{opx}	0.08–0.13	0.04–0.13	–	–
Orthopyroxene (M2)	X_{Fe}	0.27–0.33	0.27–0.31	–	–
	Y_{opx}	0.10–0.16	0.06–0.12	–	–
Biotite	X_{bi}	0.17–0.18	0.17–0.19	0.17–0.18	0.50–0.52
	Ti (wt%)	1.17–1.29	1.30–1.39	1.22–1.85	2.79–3.20
	Al (wt%)	7.87–8.36	8.27–8.68	9.09–10.09	7.49–8.03
Plagioclase	X_{ab}	–	–	0.90–0.92	0.59–0.65
	X_{an}	–	–	0.07–0.10	0.34–0.41
	X_{san}	–	–	<0.01	<0.02
Hornblende	X_{Fe}	–	–	–	0.47–0.52
Sapphirine	X_{sa}	–	0.15–0.18	–	–
	Fe3+	–	0.29–0.43	–	–
Cordierite	X_{crd}	0.05–0.09	0.01–0.08	0.08–0.19	–
Magnetite	***Cr (wt%)***	–	–	0.15–0.36	BDL–0.09
	Al (wt%)	–	–	0.07–1.13	0.12–19
	Ti (wt%)	–	–	0.31–1.38	0.02–0.05
Ilmenite	***Mn (wt%)***	–	–	0.1–0.26	0.82–0.90

Note: Unless indicated otherwise by the units (wt%), proportions are atomic/molar. $X_{gt} = Fe^{2+}/(Fe^{2+} + Mg)$. $Y_{opx} = x$ (Al,M1). $X_{alm} = Fe^{2+}/(Fe^{2+} + Mg + Ca + Mn)$. $X_{bi} = Fe^{2+}/(Fe^{2+} + Mg)$. $X_{py} = Mg/(Fe^{2+} + Mg + Ca + Mn)$. $X_{ab} = Na/(Na + Ca)$. $X_{gr} = Ca/(Fe^{2+} + Mg + Ca + Mn)$. $X_{an} = Ca/(Ca + Na + K)$. $X_{sps} = Mn/(Fe^{2+} + Mg + Ca + Mn)$. $X_{san} = K/(Ca + Na + K)$. $X_{opx} = Fe^{2+}/(Fe^{2+} + Mg)$. $X_{crd} = Fe^{2+}/(Fe^{2+} + Mg)$.

Biotite in the metamafic sample 830-23 has X_{Fe} values of 0.50–0.52. TiO_2 and Al_2O_3 concentrations are 2.79–3.20 wt% and 7.49–8.03 wt%, respectively.

4.2.5 | Amphibole

X_{Fe} values in sample 830-23 range from 0.47–0.52. Amphibole is mostly pargasitic, but from hereon will be referred to as simply hornblende.

4.2.6 | Sapphirine

X_{sa} ($Fe^{2+}/[Fe^{2+} + Mg]$) values in sample 830-7 span 0.15–0.18. Fe^{3+} concentration estimates range from 0.29–0.0.43.

4.2.7 | Feldspar

Feldspar compositions were measured in samples 830-20 and 830-23. Feldspar in both samples is dominantly albitic

TABLE 4 Electron microprobe representative mineral chemistry.

		830-6					830-7						
		Garnet core	Garnet rim	Orthopyroxene	Biotite	Cordierite	Garnet core	Garnet rim	Orthopyroxene	Biotite	Cordierite	Sapphirine	Magnetite
Oxides	SiO2	39.74	39.36	50.49	39.11	49.28	39.19	39.15	50.69	38.10	48.92	12.40	0.02
	TiO2	0.00	0.00	0.03	2.07	0.00	0.00	0.00	0.04	2.22	0.00	0.02	0.04
	Al2O3	23.36	23.12	5.99	15.46	34.62	22.63	22.55	5.30	16.11	33.41	61.79	0.29
	Cr2O3	0.00	0.00	0.00	0.00	0.00	0.00	0.00	0.00	0.00	0.00	0.11	0.07
	FeO	23.79	25.07	19.33	7.99	3.12	25.68	26.06	18.61	8.04	2.80	9.68	91.69
	MnO	0.67	0.82	0.27	0.01	0.02	0.49	0.55	0.11	0.00	0.00	0.03	0.00
	MgO	12.20	11.36	24.07	20.91	11.81	12.14	11.52	24.80	19.84	12.15	15.85	0.07
	ZnO	0.00	0.00	0.00	0.00	0.00	0.00	0.00	0.00	0.00	0.00	0.05	0.00
	CaO	1.91	1.60	0.06	0.00	0.01	0.65	0.81	0.08	0.01	0.01	0.02	0.00
	Na2O	0.00	0.00	0.00	0.34	0.05	0.00	0.00	0.01	0.39	0.06	0.00	0.00
	K2O	0.00	0.00	0.00	9.39	0.00	0.01	0.00	0.00	8.74	0.01	0.02	0.00
	Cl	0.00	0.00	0.00	0.00	0.00	0.00	0.00	0.00	0.01	0.00	0.00	0.00
	F	0.01	0.00	0.00	1.92	0.00	0.13	0.14	0.03	1.16	0.01	0.05	0.00
	H2O	0.00	0.00	0.00	3.34	0.00	0.00	0.00	0.00	3.59	0.00	0.00	0.00
	OH = cl	0.00	0.00	0.00	0.00	0.00	0.00	0.00	0.00	0.00	0.00	0.00	0.00
	OH = F	0.00	0.00	0.00	0.81	0.00	0.06	0.06	0.01	0.49	0.00	0.02	0.00
	Total	**101.69**	**101.34**	**100.26**	**96.29**	**98.92**	**100.87**	**100.72**	**99.67**	**94.25**	**97.35**	**99.35**	**92.20**
	No. oxygens	**12**	**12**	**6**	**11**	**18**	**12**	**12**	**6**	**11**	**18**	**20**	**4**
Cations	Si	2.94	2.94	1.84	2.76	4.91	2.94	2.95	1.85	2.75	4.94	1.48	0.00
	Ti	0.00	0.00	0.00	0.11	0.00	0.00	0.00	0.00	0.12	0.00	0.00	0.00
	Al	2.04	2.04	0.26	1.29	4.06	2.00	2.00	0.23	1.37	3.98	8.70	0.01
	Cr	0.00	0.00	0.00	0.00	0.00	0.00	0.00	0.00	0.00	0.00	0.01	0.00
	Fe3+	0.07	0.07	0.07	0.01	0.12	0.08	0.05	0.07	0.01	0.14	0.30	1.98
	Fe2+	1.40	1.50	0.52	0.46	0.14	1.53	1.59	0.50	0.48	0.09	0.67	1.00
	Mn2+	0.04	0.05	0.01	0.00	0.00	0.03	0.04	0.00	0.00	0.00	0.00	0.00
	Mg	1.35	1.27	1.31	2.20	1.75	1.36	1.30	1.35	2.14	1.83	2.82	0.00
	Zn	0.00	0.00	0.00	0.00	0.00	0.00	0.00	0.00	0.00	0.00	0.00	0.00
	Ca	0.15	0.13	0.00	0.00	0.00	0.05	0.07	0.00	0.00	0.00	0.00	0.00
	Na	0.00	0.00	0.00	0.05	0.01	0.00	0.00	0.00	0.05	0.01	0.00	0.00
	K	0.00	0.00	0.00	0.85	0.00	0.00	0.00	0.00	0.81	0.00	0.00	0.00
	Cl	0.00	0.00	0.00	0.00	0.00	0.00	0.00	0.00	0.00	0.00	0.00	0.00
	F	0.00	0.00	0.00	0.43	0.00	0.03	0.03	0.00	0.27	0.00	0.02	0.00

TABLE 4 (Continued)

		830-6					830-7						
		Garnet core	Garnet rim	Orthopyroxene	Biotite	Cordierite	Garnet core	Garnet rim	Orthopyroxene	Biotite	Cordierite	Sapphirine	Magnetite
	OH-	0.00	0.00	0.00	1.57	0.00	0.00	0.00	0.00	1.73	0.00	0.00	0.00
	Total	8.00	8.00	4.00	7.72	11.00	8.00	8.00	4.00	7.73	11.00	14.00	3.00

TABLE 4 (Continued)

	830-7	830-20					830-23						
	Ilmenite	Garnet core	Garnet rim	Orthopyroxene	Biotite	Cordierite	Garnet core	Garnet rim	Hornblende	Biotite	Plagioclase	Magnetite	Ilmenite
Oxides	0.12	39.65	39.25	50.49	39.11	49.28	37.58	37.46	40.02	35.50	57.62	0.04	0.00
	48.75	0.00	0.00	0.03	2.07	0.00	0.12	0.11	2.17	4.91	0.00	0.07	51.24
	0.16	23.27	23.10	5.99	15.46	34.62	20.90	20.78	12.69	14.83	25.99	0.27	0.05
	0.02	0.00	0.00	0.00	0.00	0.00	0.01	0.02	0.00	0.00	0.00	0.04	0.00
	48.12	24.17	25.33	19.33	7.99	3.12	30.93	29.97	18.94	20.03	0.06	91.48	46.96
	0.29	0.71	0.86	0.27	0.01	0.02	0.22	0.91	0.23	0.12	0.00	0.00	1.11
	1.31	11.97	11.17	24.07	20.91	11.81	3.97	4.13	8.09	10.17	0.00	0.01	0.19
	0.00	0.00	0.00	0.00	0.00	0.00	0.00	0.00	0.00	0.00	0.00	0.00	0.00
	0.01	1.85	1.50	0.06	0.00	0.01	6.17	6.34	11.31	0.01	7.87	0.00	0.00
	0.00	0.00	0.00	0.00	0.34	0.05	0.03	0.03	1.36	0.05	7.16	0.10	0.04
	0.00	0.00	0.00	0.00	9.39	0.00	0.00	0.00	1.82	9.21	0.14	0.00	0.00
	0.00	0.00	0.00	0.00	0.00	0.00	0.00	0.00	0.11	0.09	0.00	0.01	0.00
	0.00	0.01	0.00	0.00	1.92	0.00	0.02	0.02	0.08	0.12	0.02	0.00	0.00
	0.00	0.00	0.00	0.00	3.34	0.00	0.00	0.00	0.00	3.82	0.00	0.00	0.00

TABLE 4 (Continued)

	830-7	830-20					830-23						
	Ilmenite	**Garnet core**	**Garnet rim**	**Orthopyroxene**	**Biotite**	**Cordierite**	**Garnet core**	**Garnet rim**	**Hornblende**	**Biotite**	**Plagioclase**	**Magnetite**	**Ilmenite**
	0.00	0.00	0.00	0.00	0.00	0.00	0.00	0.00	0.02	0.02	0.00	0.00	0.00
	0.00	0.00	0.00	0.00	0.81	0.00	0.01	0.01	0.03	0.05	0.01	0.00	0.00
	98.79	**101.62**	**101.21**	**100.26**	**96.29**	**98.92**	**99.97**	**99.80**	**96.76**	**94.96**	**98.85**	**92.01**	**99.59**
	3	**12**	**12**	**6**	**11**	**18**	**12**	**12**	**23**	**11**	**8**	**4**	**3**
Cations	0.00	2.94	2.94	1.84	2.76	4.91	2.98	2.97	6.11	2.73	2.60	0.00	0.00
	0.92	0.00	0.00	0.00	0.11	0.00	0.01	0.01	0.25	0.28	0.00	0.00	0.97
	0.00	2.04	2.04	0.26	1.29	4.06	1.95	1.94	2.28	1.34	1.38	0.01	0.00
	0.00	0.00	0.00	0.00	0.00	0.00	0.00	0.00	0.00	0.00	0.00	0.00	0.00
	0.14	0.07	0.07	0.07	0.01	0.12	0.08	0.10	0.59	0.06	0.00	1.99	0.05
	0.87	1.43	1.52	0.52	0.46	0.14	1.97	1.88	1.83	1.22	0.00	0.99	0.94
	0.01	0.04	0.05	0.01	0.00	0.00	0.01	0.06	0.03	0.01	0.00	0.00	0.02
	0.05	1.33	1.25	1.31	2.20	1.75	0.47	0.49	1.84	1.16	0.00	0.00	0.01
	0.00	0.00	0.00	0.00	0.00	0.00	0.00	0.00	0.00	0.00	0.00	0.00	0.00
	0.00	0.15	0.12	0.00	0.00	0.00	0.52	0.54	1.85	0.00	0.38	0.00	0.00
	0.00	0.00	0.00	0.00	0.05	0.01	0.00	0.01	0.40	0.01	0.63	0.01	0.00
	0.00	0.00	0.00	0.00	0.85	0.00	0.00	0.00	0.35	0.90	0.01	0.00	0.00
	0.00	0.00	0.00	0.00	0.00	0.00	0.00	0.00	0.03	0.01	0.00	0.00	0.00
	0.00	0.00	0.00	0.00	0.43	0.00	0.00	0.01	0.04	0.03	0.00	0.00	0.00
	0.00	0.00	0.00	0.00	1.57	0.00	0.00	0.00	0.00	1.96	0.00	0.00	0.00
	2.00	8.00	8.00	4.00	7.72	11.00	8.00	8.00	15.55	7.72	5.00	3.00	2.00

with low potassium concentrations. X_{ab} (Na/[Na + Ca + K]) values are 0.90–0.92 in sample 830-20, and 0.59–0.65 in sample 830-23. X_{an} (Ca/[Na + Ca + K]) contents are 0.07–0.10 in sample 830-20, and 0.34–0.41 in sample 830-23.

4.2.8 | Ilmenite

Ilmenite in sample 830-20 has low MnO content, with values ranging from 0.1–0.26 wt%. MnO content is comparatively high in sample 830-23 ilmenite, with values of 0.82–0.90 wt%.

4.2.9 | Magnetite

Magnetite in sample 830-20 has Cr_2O_3 contents of 0.15–0.36 wt%, Al_2O_3 contents of 0.07–1.13 wt%, and TiO_2 contents of 0.31–1.38 wt%. Sample 830-23 magnetite has Cr_2O_3 contents varying between 0 and 0.09 wt%, Al_2O_3 values of 0.12–0.19 wt%, and TiO_2 contents of 0.02–0.05 wt%.

4.3 | Mineral equilibria forward modelling

Mineral equilibria forward models were calculated for samples 830-6, 830-7, 830-20, and 830-23 to supplement past pressure–temperature constraints determined via conventional thermobarometry (Scrimgeour, Close, & Edgoose, 2005).

Samples 830-6 and 830-7 contain two distinct mineral assemblages, an earlier M1 assemblage dominated by orthopyroxene and cordierite, and a later M2 assemblage characterized by the presence of garnet. The M1 assemblage is interpreted to have formed at c. 1640 Ma, coincident with the intrusion of mafic and felsic magmas (Scrimgeour, Kinny, et al., 2005). The focus of the present work is on the *P–T* conditions and timing associated with the formation of the M2 assemblage in samples 830-6 and 830-7, and the response of the accessory minerals that formed during M1 metamorphism. In contrast to samples 830-6 and 830-7, samples 830-20 and 830-23 are not obviously polymetamorphic and evaluation of their *P–T* conditions and timing aims to provide a reference frame for the M2 assemblages in the samples 830-6 and 830-7.

4.3.1 | 830-6

This sample contains two distinct mineral assemblages (Table 2). The M1 assemblage consists of coarse-grained orthopyroxene, cordierite, and quartz overprinted by coarse-grained biotite. The M2 assemblage consists of garnet, orthopyroxene, cordierite, sillimanite, biotite, ilmenite, magnetite and quartz.

Evaluating the *P–T* conditions of the M2 assemblage is subject to some circumspection, as M1 orthopyroxene forms 46% of the rock and the M2 assemblage occurs in small domains. *P–T* modelling of the M2 assemblage was performed with the M1 orthopyroxene removed from the bulk composition (Figure 5a). We recognize this is an approximation due to differences in the diffusivity of different elements (Guevara & Caddick, 2016). Nonetheless, the M1 orthopyroxene grains are large, and elements such as Al are well recognized to diffuse relatively slowly (e.g., Carlson, 2010; McFarlane et al., 2003), creating the possibility that M1 orthopyroxene grains could have become chemically isolated from the reactive bulk composition during the formation of later mineral assemblages. Removing its average composition creates a more aluminous, less Fe-Mg-rich, residual bulk composition. Using this modified bulk composition and assuming low modes of melt, plagioclase and K-feldspar are present in the rock, the M2 garnet, orthopyroxene, cordierite, sillimanite, biotite, ilmenite, quartz and melt assemblage occurs at ~8.1 kbar and 880–915°C (Figure 5a).

4.3.2 | 830-7

Similar to sample 830-6, this sample contains evidence for two distinct stages of mineral growth (Table 2). The M1 mineral assemblage is poorly preserved, but seems to be comprised of orthopyroxene, cordierite, quartz, biotite, ilmenite and magnetite. The M2 assemblage contains orthopyroxene, cordierite, biotite, ilmenite, magnetite, garnet, sillimanite, sapphirine and minor K-feldspar.

In order to model M2 metamorphism, we selected a representative domain in the sample consisting only of interpreted M2 minerals and used this to calculate an effective M2 bulk composition and *P–T* diagram (Figure 5b). This domain incorporates the formation of garnet and the cordierite-rich assemblage interpreted to have formed at the expense of garnet. Compared to the overall bulk rock composition, the reactive M2 bulk composition is more aluminous, magnesian and oxidized. Interpreting the M2 assemblage development during and subsequent to the growth of garnet has some ambiguity. Texturally, garnet predates the formation of M2 orthopyroxene and appears to have grown with sillimanite, biotite and cordierite, given their presence as inclusions. The M2 assemblage, garnet, cordierite, sillimanite, biotite, orthopyroxene, ilmenite, quartz and melt has a modelled stability between 750 and 870°C and 8.4–10.1 kbar (Figure 5b). A decrease in garnet abundance and the formation of modally minor sapphirine

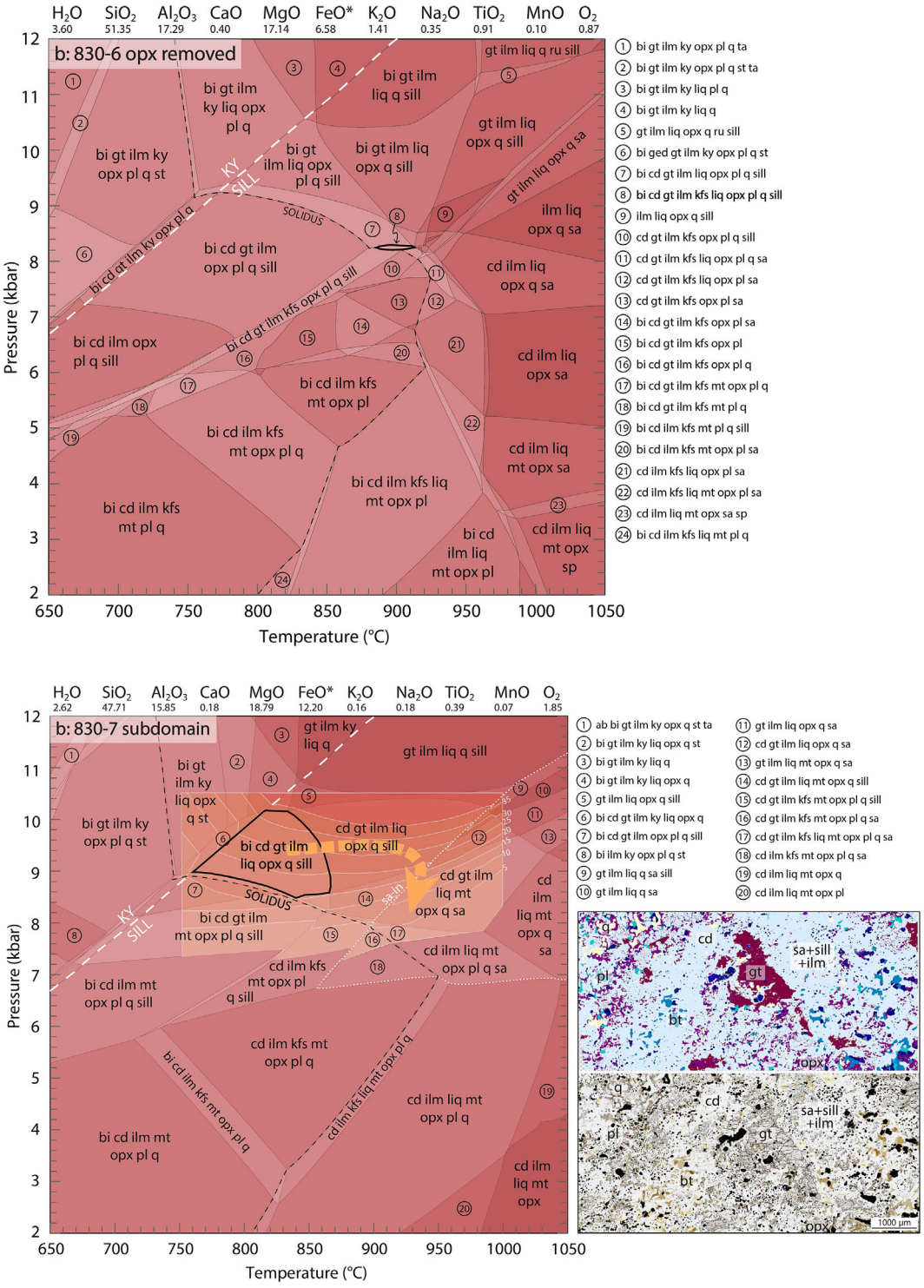

FIGURE 5 *P–T* pseudosections for samples (a) 830-6 and (b) 830-7. The black, bold outline represents the inferred peak field, and the orange arrow represents the interpreted *P–T* path. The kyanite-sillimanite phase transformation is indicated with a dashed white line, and the solidus by a dashed black line. Measured EPMA Al_2O_3 contents in wt% are overlaid on Figure 5a. Variance increases with shading in each diagram. Bulk composition used for the calculation of phase diagrams is given at the top of each model in mol%. Abbreviations: bi = biotite, cd = cordierite, gt = garnet, hb = hornblende, ilm = ilmenite, kfs = K-feldspar, ky = kyanite, melt = melt, mt = magnetite, opx = orthopyroxene, pl = plagioclase, q = quartz, ru = rutile, sa = sapphirine, sill = sillimanite, sp = spinel. Preliminary diagrams for each model are given in Appendix SB.

in the presence of cordierite is consistent with heating to at least 850°C. Modelled garnet mode contours are approximately horizontal between 750°C and 950°C and 7–10 kbar (Figure 5b). Therefore, the textural evidence of M2 garnet breakdown to a later M2 cordierite, orthopyroxene and sapphirine bearing assemblage requires some pressure decrease.

4.3.3 | 830-20

The mineral assemblage in sample 830-20 consists of garnet, sillimanite, biotite, cordierite and leucocratic patches of quartz and plagioclase. Garnet contains inclusions of rutile, staurolite and kyanite, and matrix prismatic sillimanite and quartz contain inclusions of rutile, ilmenite, and biotite. Together, this suggests the rock traversed staurolite-bearing *P–T* space, intersected kyanite-sillimanite stability in its early history, and eventually evolved to contain the assemblage garnet, sillimanite/kyanite, quartz, plagioclase, rutile, ilmenite, biotite and melt. For the modelled bulk composition, this assemblage is stable between 710°C and 830°C and 7.6–10.1 kbar. Texturally, matrix biotite predominantly appears to postdate sillimanite, but predates the formation of cordierite suggesting the rock evolved to stabilize garnet, ilmenite, melt, plagioclase, quartz, sillimanite and potentially biotite. This assemblage is modelled to be stable between 700°C and 830°C and 6.6–8.7 kbar (Figure 6a). The subsequent formation of cordierite and minor K-feldspar at the limited expense of biotite, sillimanite and garnet indicates the rock evolved to pressures of <6.5 kbar. Therefore, the overall suggestion is the rock followed a generally pressure decreasing path as the matrix foliation evolved.

4.3.4 | 830-23

The peak mineral assemblage is garnet, hornblende, biotite, ilmenite, plagioclase, K-feldspar and melt (Figure 6b). Very rare titanite occurs in the sample but does not appear in the *P–T* model. This may reflect a localized composition not representative of the modelled overall bulk composition, or alternatively *a–x* models that are not tailored to the mineral chemistries. Garnet mode contours are comparatively flat in *P–T* space, and the modelled peak assemblage with interpreted garnet abundance occurs at pressures of 9 kbar and at temperatures between ~750°C and 850°C. The reduction in garnet mode associated with the formation of biotite and hornblende is consistent with pressure decrease accompanying melt crystallization. Based on the present garnet mode (8%) compared to that inferred for the metamorphic peak (9.5%), ~1 kbar of pressure drop may be recorded by the sample. Temperatures are less well constrained. Coarse-grained garnet (>1 cm) preserves prograde zoning with elevated Mn and comparatively low Fe concentrations in the core. These decrease and increase respectively rimward, however the average FeO concentration is 30.5 wt%. Modelled FeO contours in the peak field form a circular distribution, with the overall measured FeO value centred on 815°C (Figure 6b). A retrograde evolution is tentatively inferred based on the decreased mode of garnet, and increased modes of plagioclase, biotite and ilmenite.

4.4 | Geochronology

4.4.1 | HT mg-rich granulites

U–Pb monazite geochronology

Monazite in sample 830-6 is locally abundant in M2 reaction domains. However, most of these grains are too small (<5 μm) to analyse. The analysed monazite ranges in size from 40 to 250 μm with typical aspect ratios of 1:3. Grains are usually anhedral, and BSE zoning is weak to non-existent. Fifteen monazite grains were analysed in sample 830-6, most of which occur within M1 biotite, or at the rims of coarse-grained M1 orthopyroxene where they are partially exposed to the predominantly M1 matrix assemblage. One grain is fully enclosed within M1 orthopyroxene. Ninety-two analyses yield two populations (Figure 7a). Seventy-three concordant analyses from the oldest population yield $^{207}Pb/^{206}Pb$ dates between 1688 and 1509 Ma and cluster on a probability density plot at c. 1630 Ma. Outside of this older population, a secondary probability density peak is recorded at c. 1200 Ma. Mesoproterozoic dates are exclusively derived from a single monazite inclusion inside M1 orthopyroxene. REE compositions for concordant 830-6 monazite (Appendix SD) are consistent across all textural locations with Eu anomalies of ~0.26, and negative HREE slopes with Gd_N/Yb_N between 11.97 and 58.40 (mean $Gd_N/Yb_N = 37.43$).

Monazite analysed in sample 830-7 is anhedral to subhedral and between 40 and 200 μm, although abundant fine-grained monazite (<5 μm) is also present (Appendix SB). Grains are unzoned or weakly zoned in BSE images. Forty-four monazite grains were analysed from various textural locations within the matrix or hosted in garnet or M1 orthopyroxene with a total of 256 analyses. Of the 256 analyses, 197 are concordant and yield a continuous span of dates from c. 1740–1153 Ma. The majority of analyses define peaks on a probability density plot at c. 1630 Ma and c. 1600 Ma, together with concordant analyses that track towards

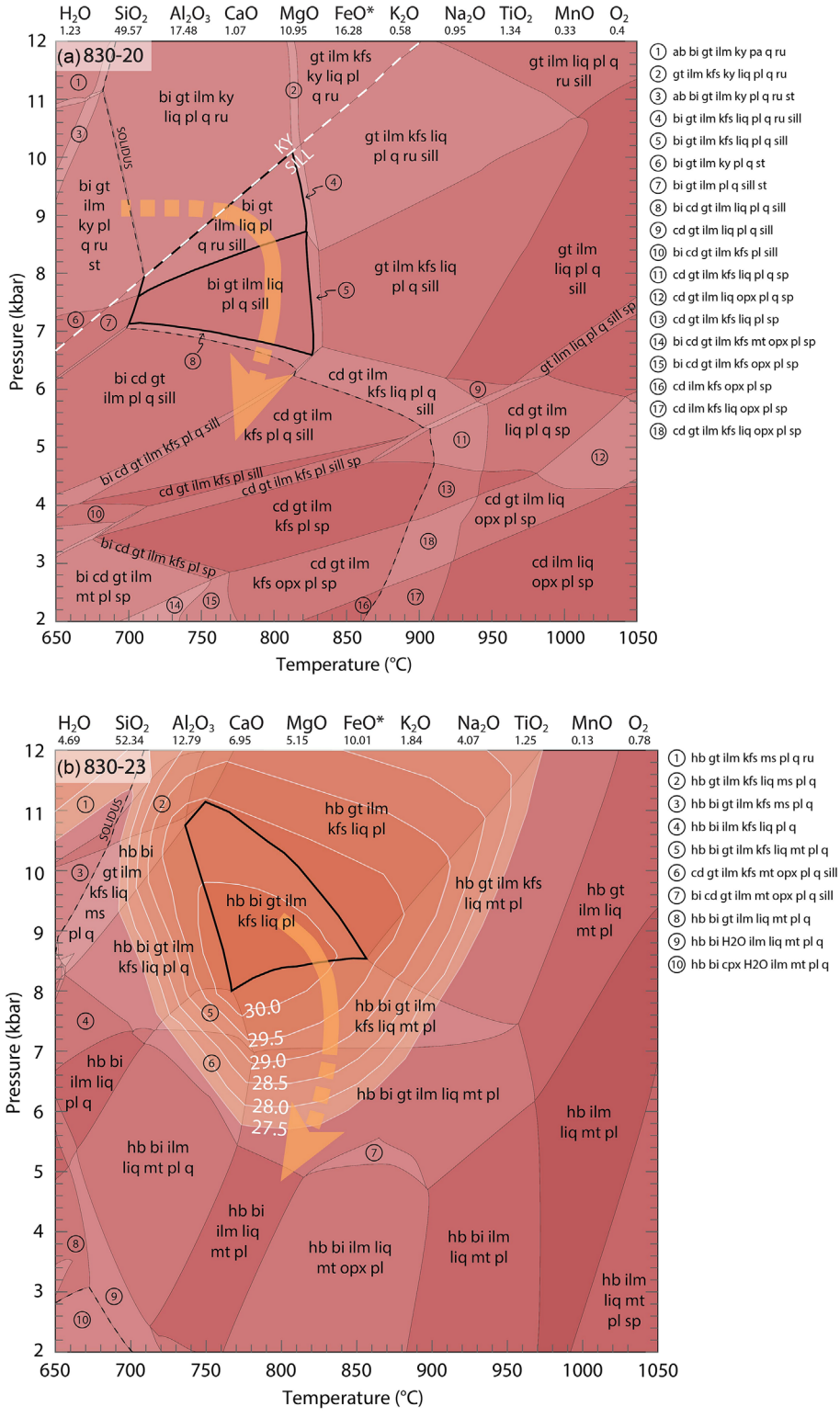

FIGURE 6 *P–T* pseudosection for samples (a) 830-20, and (b) 830-23. Garnet FeO concentrations in wt% are overlaid on Figure 6b. Abbreviations and annotations are detailed in Figure 5.

c. 1150 Ma. There is no correlation between textural location and age. REE compositions in sample 830-7 are broadly uniform for all concordant analyses, with a slight Eu anomaly (~0.39) and Gd_N/Yb_N spanning from 11.30–141.64 (mean $Gd_N/Yb_N = 40.66$). Younger concordant analyses are slightly more enriched in HREEs than older monazite (Appendix SD).

U–Pb zircon geochronology and REE compositions

The analysed zircons from sample 830-6 are typically ~50–150 μm in length (aspect ratio = 1:3–1:4), and subhedral to euhedral. Zoning expressed in CL images is usually subtle and irregular, with occasional bright cores, and rare instances of oscillatory zoning (Figure 8a). There is no obvious correlation between zoning and $^{207}Pb/^{206}Pb$

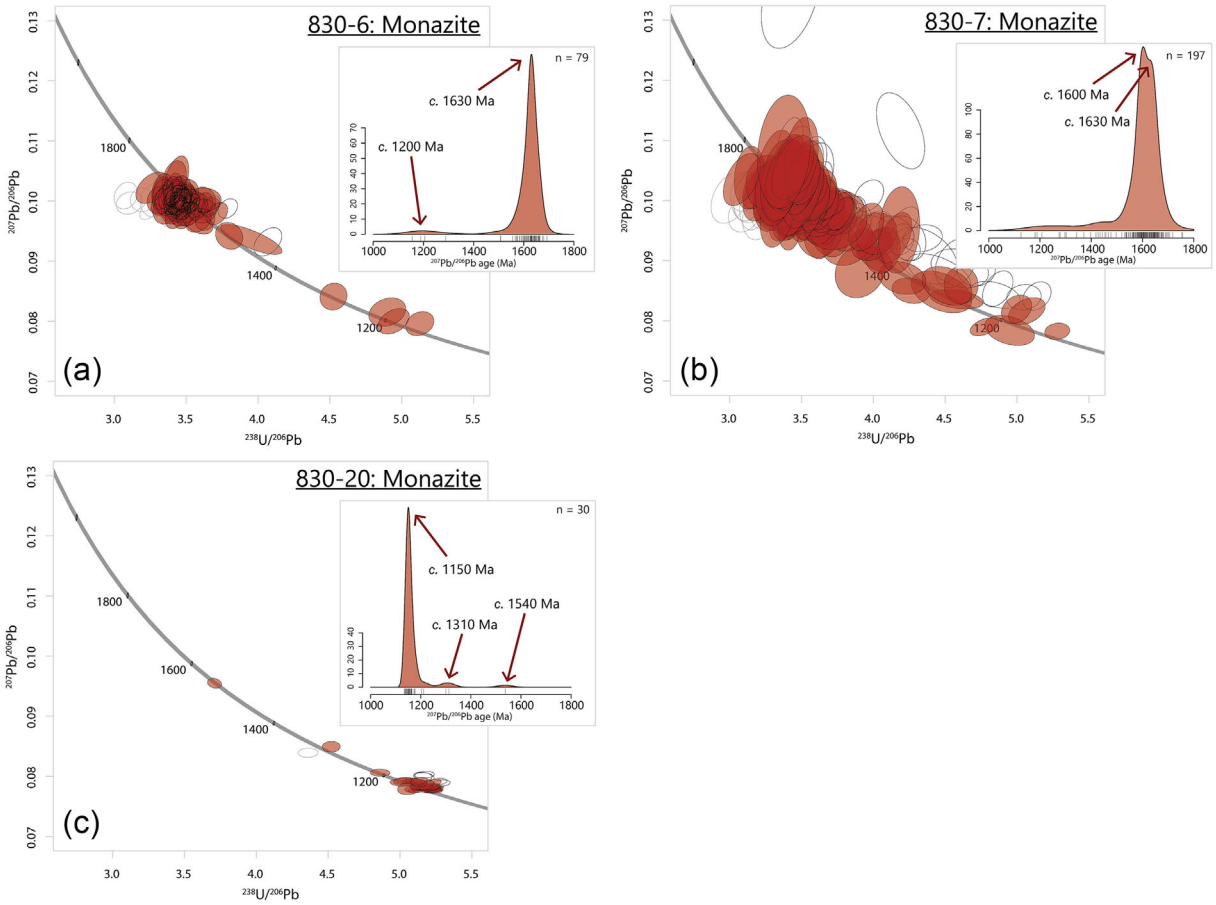

FIGURE 7 U–Pb monazite Tera Wasserburg concordia plots. Coloured ellipses indicate concordant data. Probability density plots for $^{207}Pb/^{206}Pb$ ages are provided as insets for each sample. (a) 830-6, (b) 830-7, (c) 830-20, inset figure magnifies the Mesoproterozoic population. Only concordant analyses were used in the calculation of probability density plots, where concordance is defined as being within 2σ uncertainty of concordia.

dates. LA–ICP–MS results from 146 analyses collected from 38 zircons yielded 106 concordant analyses. Concordant analyses span 1684–1572 Ma and give a $^{207}Pb/^{206}Pb$ weighted mean date of 1637 ± 6 Ma ($n = 106/146$; MSWD = 1.05; Figure 9a). Concordant analyses have consistent REE trends with limited dispersion, characterized by a slightly negative Eu anomaly (mean $Eu_N/\sqrt{[Sm_N{*}Gd_N]} = 0.25$), positive HREE slopes with Lu_N/Gd_N ranging from 8.66–19.26 (mean $Lu_N/Gd_N = 12.67$) and Th/U of 0.12–1.59 (mean Th/U = 1.00). Zircon trace element concentrations have been ratioed against garnet and compared to experimentally determined zircon/garnet REE partition coefficients (Kd; Figure 10a; Rubatto, 2002). Zircon trace element compositions for the 1660–1500 Ma aged zircons are divided by representative, averaged garnet core and rim trace element compositions. The average result is represented by a bold line, and the full range in ratios by an envelope. There is ambiguity in this approach, increased by garnet in sample 830-6 being coronitic and not abiding by classic core to rim growth. Regardless of the accuracy of this assignation, there is limited variability in rare earth element composition across different zircon analyses when divided by garnet. Similarly, although garnet is slightly zoned in almandine, grossular and spessartine, there is no significant difference in K_D values between garnet cores and rims relative to zircon. Excluding La, the ratio of REEs in zircon relative to garnet exceeds one for all elements, indicating zircon is enriched in REEs compared to garnet.

In sample 830-7, the analysed zircon grains are 30–125 μm in size (aspect ratio = 1:3) and subhedral. CL zoning is patchy, irregular, and shares no relationship with age (Figure 8b). Fifty-eight analyses were collected from 24 grains, of which 46 are concordant. Concordant $^{207}Pb/^{206}Pb$ dates span 1800–1,567 Ma. Rejecting one outlier, sample 830-7 yields a weighted mean $^{207}Pb/^{206}Pb$ age of 1672 ± 13 Ma for concordant analyses, likely reflecting combined detrital and metamorphic zircon results ($n = 45/46$; MSWD = 0.60; Figure 9b; e.g., Scrimgeour,

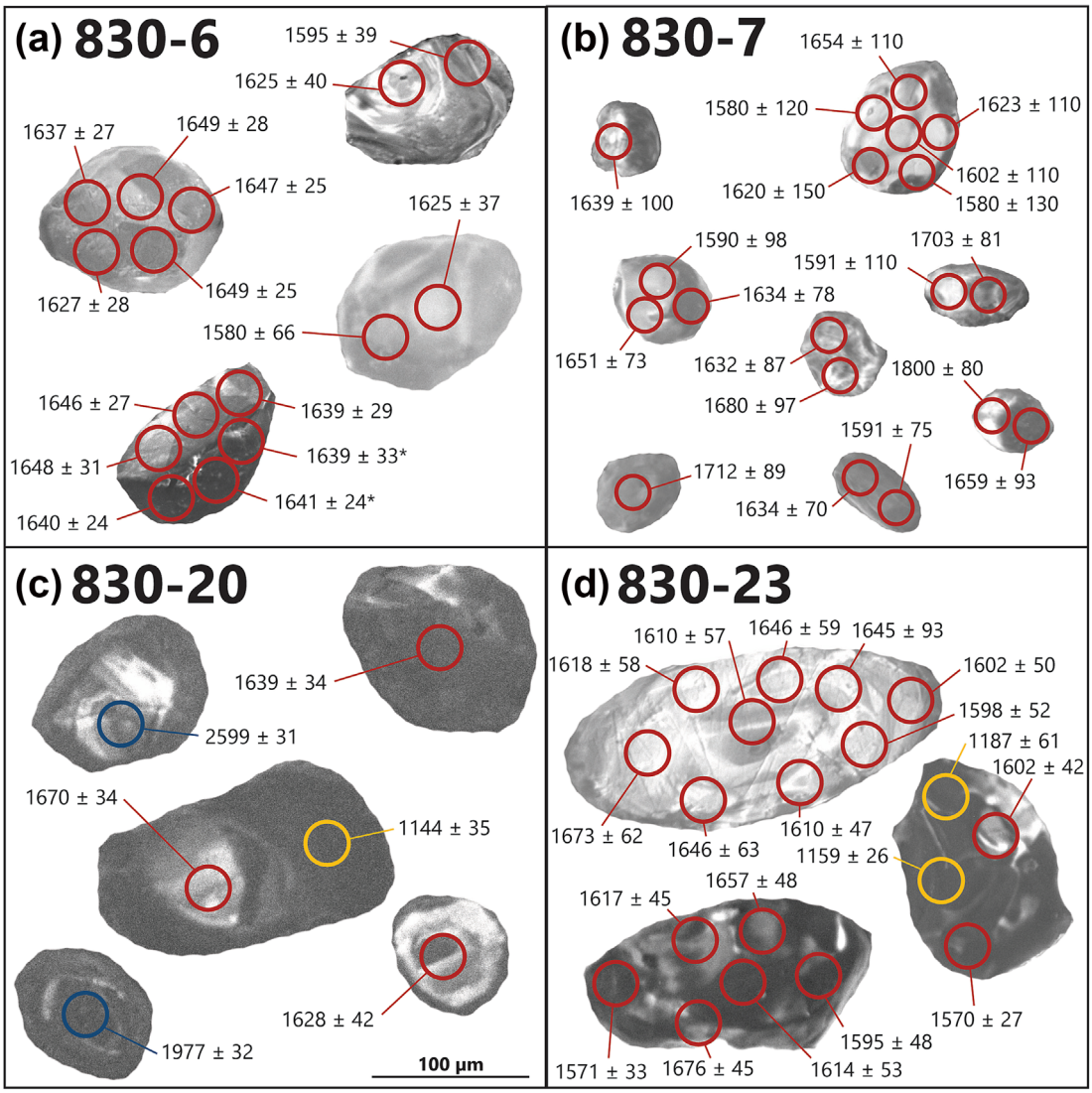

FIGURE 8 Representative examples of zircon SEM-CL zoning in samples (a) 830-6, (b) 830-7, (c) 830-20 and (d) 830-23. Ages are in Ma. <1200 Ma analyses are given in yellow, 1800–1570 Ma analyses in red and >1900 Ma analyses in blue. Discordant analyses are indicated by an asterisk.

Kinny, et al., 2005). REE signatures for concordant 830-7 zircon analyses are not correlated with age and are broadly uniform, with depleted LREEs, subtle Eu anomalies (~0.38), positive slopes in HREEs with Lu_N/Gd_N ranging from 9.54–46.22 (mean $Lu_N/Gd_N = 17.95$), and Th/U between 0.07 and 2.36 (mean Th/U = 1.13). Similar to sample 830-6, zircon-garnet K_D values in sample 830-7 show consistent enrichment across all REEs in zircon relative to garnet, both for garnet rims and cores (Figure 10b).

Lu–Hf garnet geochronology

Five garnet grains of variable size (< 1 cm) were analysed from sample 830-6. Lu concentrations are low (Table S6) with a maxima of 3.0 ppm, but are generally less than 1.5 ppm. These low concentrations necessitated a large laser spot size in order to generate useable data. To compensate for the very low concentrations of Lu, a large number of analyses (408) were obtained. These give an isochron age of 1135 ± 39 Ma ($n = 408$; MSWD = 2.7; Figure 11b), with $^{176}Lu/^{177}Hf$ spanning 0.06–14.39.

4.4.2 | Migmatitic rocks

U–Pb monazite geochronology

Monazite grains in sample 830-20 vary in size from 50 to 300 µm and are dominantly anhedral. Most grains exhibit weak CL/BSE zoning with darker cores. Twenty-four grains were identified in thin section, where all exist in the matrix except for one that occurs as an inclusion inside garnet. Forty-eight analyses were obtained, of

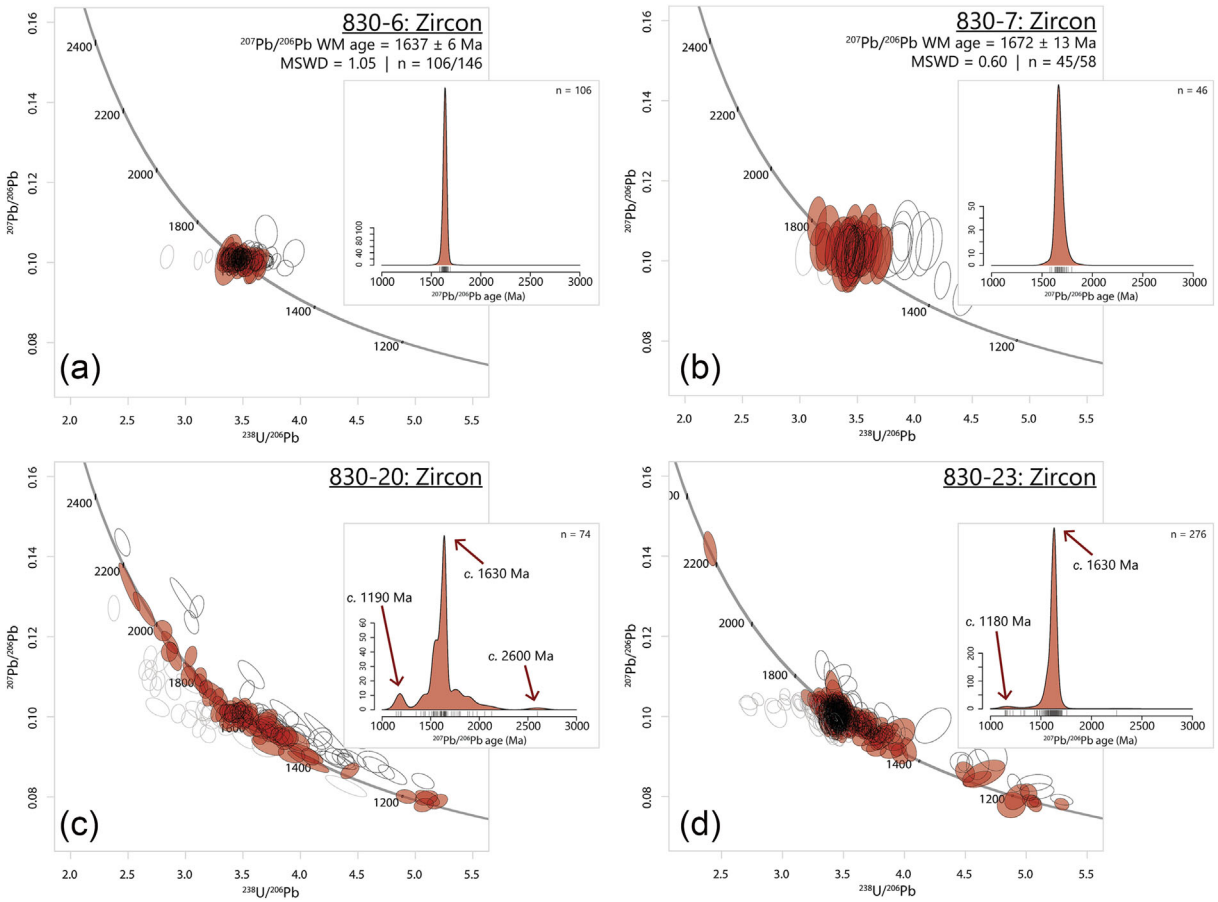

FIGURE 9 U–Pb zircon Tera Wasserburg concordia plots. Coloured ellipses indicate concordant data. Probability density plots for concordant $^{207}Pb/^{206}Pb$ ages are provided as insets for each sample (a) 830-6, (b) 830-7, (c) 830-20, (d) 830-23. Only concordant analyses were used in the calculation of probability density plots, where concordance is defined as being within 2σ uncertainty of concordia.

which 30 are concordant. Concordant analyses yield dates of 1536–1134 Ma, clustering at c. 1150 Ma on a probability density plot, with minor peaks at c. 1310 Ma and c. 1540 Ma (Figure 8c). Excluding one Paleoproterozoic outlier, ages from core to rim of monazite grains span an equivalent age range. Monazite exhibits a subtle Eu anomaly (~0.57). HREEs are variably enriched and do not share a relationship with age (Appendix SD).

U–Pb titanite geochronology

Two coarse-grained (~1000 μm) porphyroblasts of titanite were analysed from sample 830-23. These are the only grains identified in thin section. 70 analyses were obtained, all of which contain variable amounts of common and radiogenic Pb, defining a discordia line (Figure 12). The lower intercept of this discordia gives a poorly defined date of 1125 ± 8 Ma ($n = 70/70$; MSWD = 2.10). Titanite is slightly more enriched in LREEs relative to HREEs and exhibits a strongly positive Eu anomaly (~14.58; Appendix SE).

U–Pb zircon geochronology

Zircon in sample 830-20 is fine-grained (25–125 μm), typically has a 2:1 aspect ratio, and is either irregularly or sector zoned in CL images (Figure 8c). Detrital, >2 Ga ages typically come from dark, sector zoned cores rimmed by a thin, bright zone. Aside from this, there are no diagnostic zoning patterns to differentiate between Paleoproterozoic and Mesoproterozoic zircon. The 139 analyses were collected from 108 zircon grains, of which 74 are concordant. Concordant analyses yield a range of dates from c. 2120 Ma to 1144 Ma (Figure 9c). These analyses define a minor peak at c. 2600 Ma, a broad peak at c. 1630 Ma, and a minor peak at c. 1190 Ma (Figure 9c, inset). Paleoproterozoic concordant analyses are variably depleted in LREEs, exhibit negative Eu anomalies ranging from 0.09–0.78, positively sloped HREEs with Lu_N/Gd_N between 13.36–188.43 (mean $Lu_N/Gd_N = 65.93$; $n = 45$), and Th/U spanning 0.01–0.56 (mean Th/U = 0.19). Comparatively, concordant Mesoproterozoic-aged analyses defining the lower

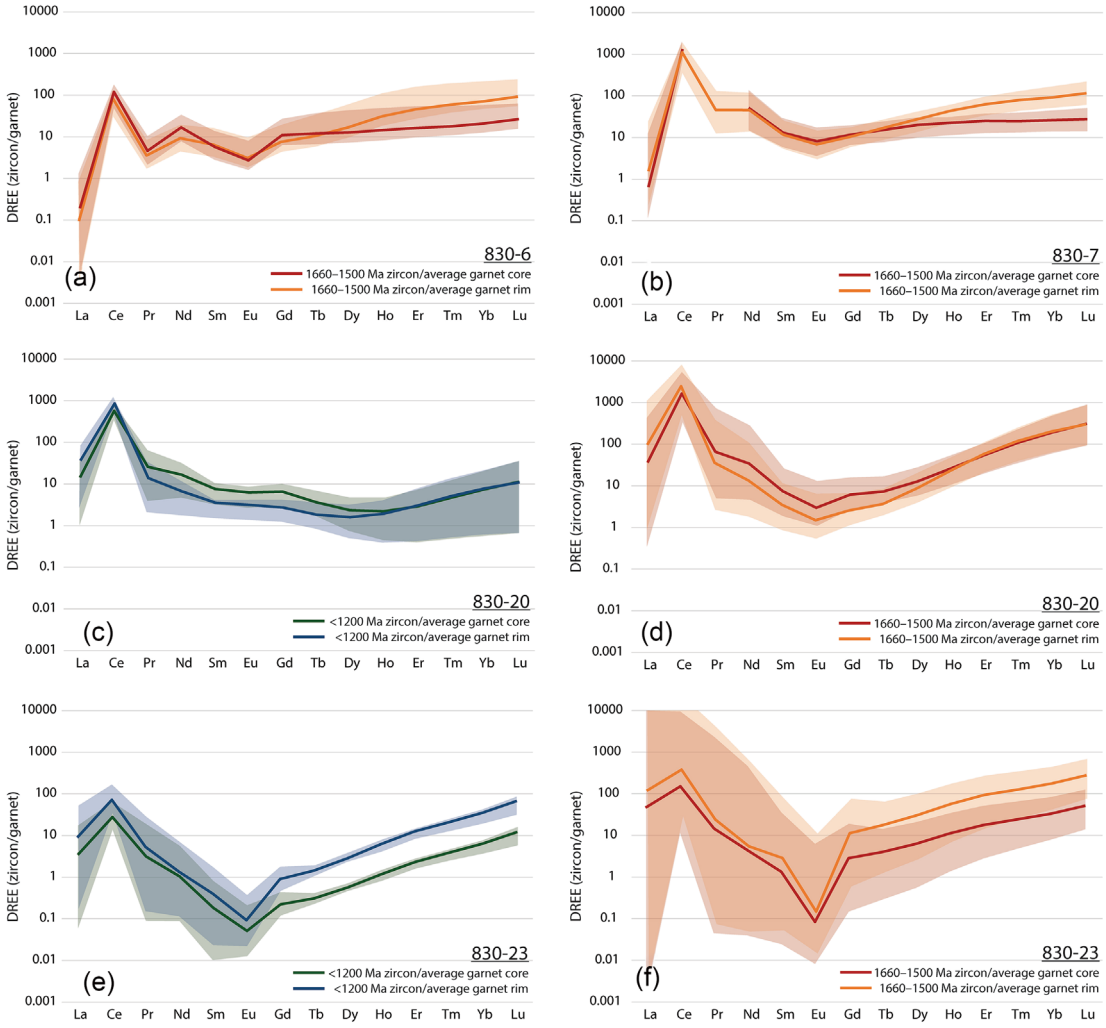

FIGURE 10 Zircon-garnet rare earth element ratios for average Liebig- (1660–1500 Ma) and Musgrave-aged (<1200 Ma) zircons relative to representative garnet cores and garnet rims. Envelopes are used to represent the full range in zircon compositions for each age population. (a) Sample 830-6 Liebig-aged zircon and garnet. (b) Sample 830-7 Liebig-aged zircon and garnet. (c) Sample 830-20 Musgrave-aged zircon and garnet. (d) Sample 830-20 Liebig-aged zircon and garnet. (e) Sample 830-23 Musgrave-aged zircon and garnet. (f) Sample 830-23 Liebig-aged zircon and garnet. Red = Liebig-aged zircon/garnet cores, orange = Liebig-aged zircon/garnet rims, green = Musgrave-aged zircon/garnet cores, blue = Musgrave-aged zircon/garnet rims.

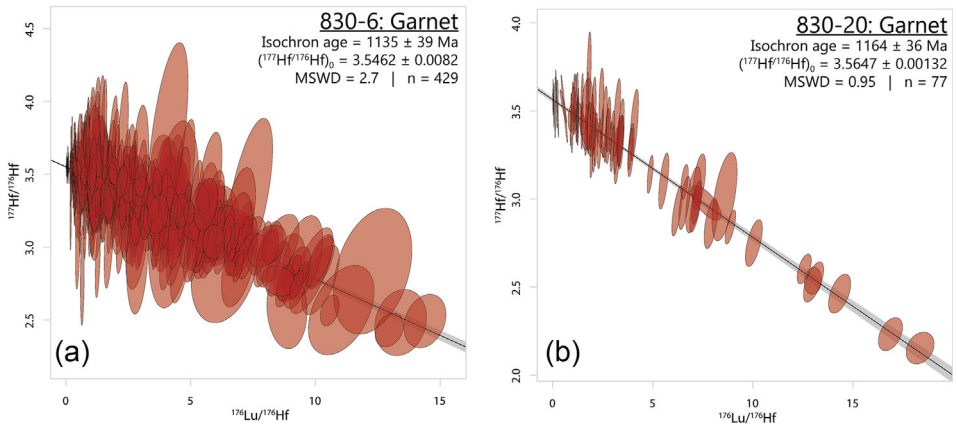

FIGURE 11 Lu–Hf garnet isochron plots. (a) 830-6, (b) 830-20.

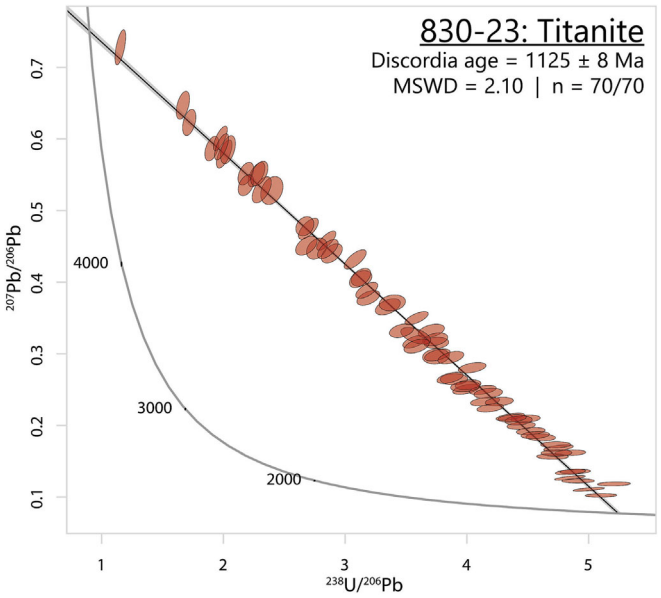

FIGURE 12 U–Pb titanite Tera Wasserburg concordia plot.

intercept cluster are more depleted in LREEs, lack Eu anomalies, and have flatter HREEs with Lu_N/Gd_N spanning 0.17–9.30 (mean $Lu_N/Gd_N = 2.67$; $n = 5$). Th/U for these Mesoproterozoic-aged grains ranges from 0.01–0.05 (mean Th/U = 0.03). Zircon trace element compositions for sample 830-20 were measured for both Paleoproterozoic (1660–1500 Ma) and Mesoproterozoic (<1200 Ma) zircon and compared to representative garnet core and rim trace element compositions. On average, Mesoproterozoic zircon is comparatively enriched in HREEs relative to garnet cores and rims, although for some zircon/garnet ratios below 1 are calculated (Figure 10c). For HREEs spanning from Dy to Lu, Paleoproterozoic zircon is systematically enriched relative to garnet cores and rims, with all ratios exceeding 1 (Figure 10d).

Zircon in sample 830-23 is subhedral to euhedral, and between 75 and 250 μm in size. Zoning is predominantly irregular, with occasional sector or oscillatory zoning in some grains. LA–ICP–MS data was collected for 333 analyses from 144 grains, of which 276 are concordant (Figure 9d). One early Paleoproterozoic $^{207}Pb/^{206}Pb$ age of 2246 ± 43 Ma was obtained. The majority of analyses define a peak at c. 1630 Ma, with a secondary minor peak at c. 1180 Ma (Figure 9d, inset). REE compositions for concordant analyses in sample 830-23 transition from being HREE-enriched to progressively more depleted with decreasing age (Appendix SF). Eu_N/Eu^*(~0.20), the slope of HREEs (Lu_N/Gd_N = 5.18–208.18), and Th/U (Th/U = 0.02–2.71) do not vary systematically with age. Zircon-garnet trace element composition ratios for Paleoproterozoic and Mesoproterozoic zircon relative to garnet cores and rims (Figure 10e,f) shows that zircon is enriched in HREEs relative to garnet in all scenarios.

Lu–Hf garnet geochronology

Two coarse-grained garnet (~3 cm) were analysed from sample 830-20. Seventy-seven spots were placed across both garnet cores and garnet rims, yielding a Lu–Hf isochron age of 1164 ± 36 Ma ($n = 77$; MSWD = 0.95; Figure 11a). Analysis of separate garnet for trace elements measured Lu concentrations of up to 3.4 ppm (Table S6), resulting in $^{176}Lu/^{177}Hf$ of up to 18.

5 | DISCUSSION

5.1 | Metamorphic evolution of *HT* Mg-rich granulites

High-temperature samples 830-6 and 830-7 are both Mg- and Al-rich, Si-depleted metapelitic rocks. Petrologically, both samples contain two distinct mineral assemblages. The M1 assemblage is variably preserved and consists of coarse-grained orthopyroxene, cordierite, and biotite, together with quartz, ilmenite and magnetite. The second assemblage (M2) is defined by the formation of garnet, which contains abundant inclusions of sillimanite, together with cordierite and biotite.

M1 conditions are suggested to be comparatively low-pressure and high temperature based on the presence of coarse-grained orthopyroxene and cordierite porphyroblasts in samples 830-6 and 830-7, as well as abundant, well-preserved sillimanite pseudomorphs after euhedral cm-sized andalusite in aluminous, orthopyroxene-free M1assemblages (Figure 3a), pointing to a low-pressure prograde M1 evolution. This could be explained by the intrusion of mafic magmas and subsequent contact metamorphism in surrounding country rocks. The gabbro body adjacent to the domain of *HT-UHT* rocks (Figure 1) is an example of one of these mafic intrusions in the Warumpi Province that intruded at c. 1640 Ma (Scrimgeour, Close, & Edgoose, 2005; Scrimgeour, Kinny, et al., 2005), as recorded in the zircon geochronology in sample 830-23 (Figure 9d). While the outcropping gabbroic body adjacent to samples 830-6 and 830-7 is modest in size, it may have formed part of a larger body whose cumulative emplacement led to a significant increase in temperature over time and the generation of granulite conditions in wall rocks that prograded through the andalusite field (e.g., McFarlane et al., 2003; McFarlane & Harrison, 2006; Nabelek et al., 2012), resulting in the formation of metamorphic zircon rims at c. 1640 Ma (Scrimgeour, Kinny, et al., 2005).

In both samples 830-6 and 830-7, the M2 assemblages are domainal. In sample 830-6, the volume of M2 recrystallisation is comparatively small, whereas in sample 830-7 at least 50% of the rock recrystallised during M2. *P–T* modelling of bulk compositions that only comprise M2 mineral assemblages in samples 830-6 and 830-7 give peak conditions of ~8–10 kbar and ~850–915°C. The initial stages of the M2 assemblage development involved the growth of sillimanite, which was then followed by the formation of garnet. Subsequently, cordierite, orthopyroxene, and/or sapphirine developed at the expense of garnet. In a rock initially containing cordierite, and without sillimanite and garnet, this mineralogical evolution suggests M2 followed a generally clockwise *P–T* evolution that culminated in *HT* to *UHT* granulite facies conditions.

U–Pb monazite and zircon ages from these *(U)HT* samples are mostly between 1700 and 1600 Ma, broadly associated with the c. 1640 Ma Liebig Orogeny (Close et al., 2005; Scrimgeour, Close, & Edgoose, 2005; Scrimgeour, Kinny, et al., 2005). U–Pb data from monazite in both *(U)HT* metapelitic samples are largely Paleoproterozoic, though with some evidence for Pb loss during the Mesoproterozoic. If the concordant monazite analyses from samples 830-6 and 830-7 are combined, Gaussian decomposition predicts 87% of the analyses ($n = 270$), define a population with an apparent age of 1614 ± 3 Ma. This broadly aligns with the c. 1640 Ma Liebig Orogeny. Monazite is only rarely inherited into metamorphic rocks as detrital grains and is understood to more readily undergo coupled dissolution in fluid-rich environments present during prograde metamorphism of metasedimentary rocks (e.g., Rasmussen et al., 2006; Yang & Pattison, 2006). Therefore, the monazite ages in these samples are interpreted to reflect the timing of M1 metamorphism, giving ages similar to Scrimgeour, Kinny, et al. (2005).

Concordant U–Pb zircon ages define a broad spread from 1800 to 1567 Ma, with the modal peak in the distribution across samples 830-6 and 830-7 occurring at c. 1630 Ma (Figure 9a,b). Interpreting these ages in terms of metamorphism is problematic, as their cumulative range is unlikely to reflect the duration of a single thermal event. In the samples analysed in this study there is no obvious relationship between zircon composition, morphology, and age which could be used to distinguish detrital grains from new zircon growth or Pb loss during a thermal event at c. 1630 Ma. However, from the same domain of low strain *HT-UHT* rocks, Scrimgeour, Kinny, et al. (2005) interpreted detrital zircons to be as young as c. 1660 Ma. These detrital grains were overgrown by rims that formed at c. 1640 Ma, interpreted to record the timing of metamorphism (Scrimgeour, Kinny, et al., 2005). In this study, this phase of metamorphism has been assigned M1. Although concordant zircon analysed in this study spans a broad range of ages, the modal peak in the distribution across samples 830-6 and 830-7 occurs at c. 1630 Ma. This is almost identical to the metamorphic zircon age reported by Scrimgeour, Kinny, et al. (2005). The inferred existence of detrital zircons only marginally older than the c. 1640–1630 Ma age inferred for metamorphism (Scrimgeour, Close, & Edgoose, 2005; Scrimgeour, Kinny, et al., 2005), mean Pb loss at c. 1630 Ma would result in concordant, yet marginally older, ages that could be difficult to distinguish from new metamorphic zircon growth. Therefore, while the c. 1630 Ma age population dominates the zircon U–Pb data, the precise status of the range in zircon ages is unclear.

At face value, the prevalence of Paleoproterozoic ages from monazite and zircon U–Pb geochronology—both within this study and in past work (Scrimgeour, Close, & Edgoose, 2005; Scrimgeour, Kinny, et al., 2005)—would be interpreted to constrain the timing of *HT–UHT* metamorphism. However, petrographic observations in combination with *P–T* modelling show this *(U)HT* assemblage is associated with the formation of garnet and the overprinting of an earlier lower-pressure, *HT* assemblage. This contributes ambiguity as to whether the c. 1630 Ma age signature is associated with the M1 or M2 event.

Paleoproterozoic-aged zircon is systematically enriched in HREEs relative to M2 garnet in samples 830-6 and 830-7 (Figure 10). This suggests zircon crystallization pre-dates—and does not appear to overlap at all, with—*HT-UHT* garnet growth in the samples. Typically, Lu contents of garnet are less than 1 ppm, whilst zircon is comparatively enriched and typically contains >60 ppm Lu (Tables S4 and S6). Lu–Hf geochronology from sample 830-6 attempts to quantify the age difference between zircon and M2 garnet. The in-situ garnet Lu–Hf data defines an isochron age of 1135 ± 39 Ma, with a corresponding MSWD of 2.7 (Figure 11). Despite adopting a utilitarian approach and collecting >400 garnet spot analyses, the precision of this age remains low due to the preferential sequestration of HREEs (including Lu) into early zircon, resulting in garnet with low Lu concentrations, amounting to low Lu/Hf ratios that limit precision. We have triaged the Lu–Hf data for inherited Zr and other mineral inclusion contaminants, but recognize that the data remains over-dispersed and the uncertainty is likely underestimated.

The diffusional behaviour of Lu–Hf in garnet has been evaluated both theoretically and empirically in past works, with various factors influencing systematics. These include 'younging' effects associated with inherited Hf-rich zircon (Scherer, Cameron, & Blichert-Toft,

2000), preferential partitioning of Lu in garnet cores versus rims and resultant weighting of ages towards core nucleation (e.g., Hollister, 1966; Kohn, 2009; Lapen et al., 2003; Skora et al., 2006), and the greater mobility of Lu relative to Hf, causing ages to be skewed younger or older depending on post-growth processes (e.g., Bloch et al., 2015, 2020; Bloch & Ganguly, 2015; Kelly et al., 2011; Kohn, 2009; Smit et al., 2013). We have attempted to consider the first of these factors by examining the relationship between $^{176}Lu/^{176}Hf$ concentrations relative to Zr, and excluding Zr-rich analyses (>100 ppm). Zoning patterns in Lu cannot be adequately accounted for due to M2 garnet in sample 830-6 occurring as coronas that undergo lateral crystallization rather than a classic porphyroblastic style of growth. Additionally, analysis was conducted in situ with spot analyses spread across garnet grains and not via dissolution. Existing data on the relative diffusivities of Lu and Hf suggests modification of the garnet Lu–Hf system will be more overtly controlled by Lu mobility. Based on this theory and depending on the post-growth processes that may affect garnet (at temperatures where Lu is mobile), Lu concentrations can (1) homogenize within garnet, (2) decrease if a high-temperature Lu compatible reservoir forms in the surrounding matrix or (3) increase if garnet is the primary Lu reservoir and its volume reduces. The latter two cases in particular have the potential to significantly affect the derived Lu–Hf age (Bloch et al., 2015; Bloch et al., 2020; Bloch & Ganguly, 2015; Briqueu et al., 1984). If Lu is lost to the matrix, the Lu–Hf age will be older than the growth. Conversely, if Lu concentrates into garnet during garnet resorption (akin to Mn concentration in resorbed garnet), there is potential for the derived Lu–Hf age to be younger than the growth age due to the excess of Lu. In a scenario where garnet may have experienced Lu resorption or diffusion, the larger the time difference between when the garnet initially grew and when Lu loss or gain occurred, the greater the resultant age modification. Bloch and Ganguly (2015), Bloch et al. (2015) examined these various affects in a series of simulations. In general terms, their results show a 'critical grain size' exists for garnet, where radii above this value do not experience significant Lu–Hf age modification. In a scenario where garnet experienced 20 Myr of prograde heating and an initial cooling rate of 4°C/Myr, deviations from the 'true' Lu–Hf growth age are minimal and asymptotically approach zero for radii exceeding ~300 μm. The analysed M2 garnet in sample 830-6 range in size from 1000 to 3000 μm and have been partially replaced by post-peak M2 cordierite-orthopyroxene. Conceivably, the reduction in garnet volume could have led to Lu enrichment, resulting in an age younger than the growth age. However, unlike sample 830-7, the extent of garnet resorption in sample 830-6 is minor and it is unlikely the Lu–Hf age could be substantially younger than the growth age. Despite the aforementioned models predicting significant Lu mobility, empirical studies indicate natural garnet may behave differently. Garnet in the sole of the Omani Ophiolite was subject to peak conditions of 850°C and 11–13 kbar, but contrary to the predicted modelled mobility of Lu, retained well-preserved growth zoning (Guilmette et al., 2018). Additionally, past works have noted a synchronicity between U–Pb and Lu–Hf geochronology in *(U)HT* rocks (e.g., Johnson et al., 2018), potentially suggesting the preferential mobility of Lu and retention of Hf may not affect high-temperature systems to the extent indicated in theoretical models (e.g., Bloch et al., 2015; Bloch & Ganguly, 2015).

Regardless, the apparent 'age' for garnet in sample 830-6 is ~500 Myr younger than the bulk U–Pb ages for zircon and monazite, although the measured overdispersion means the possibility of older, inherited garnet cannot be entirely excluded on the basis of Lu–Hf results alone. However, the textural context of garnet as a constituent of the M2 assemblage where it forms large-scale coronas around M1 orthopyroxene (Figure 3c and 4e) in combination with the preferential partitioning of HREEs into c. 1630 Ma zircon (Figure 10a,b) provides a firm foundation to suggest the garnet, and therefore, the M2 assemblage is Mesoproterozoic in age.

Although we will not attempt to constrain the onset or duration of the temperature regime associated with garnet growth, the calculated Lu–Hf age does coincide with the Musgrave Orogeny, a transcontinental-scale, high-temperature orogenic system in southern central Australia (e.g., Tucker et al., 2015) that also affected the Warumpi Province (Morrissey et al., 2011; Wong et al., 2015).

5.2 | Metamorphic evolution of migmatitic rocks

Migmatitic samples 830-20 and 830-23 come from the regional-scale rock system that encloses the low-strain, *HT-UHT* rocks. Relative to the *(U)HT* samples, these rocks contain texturally simple peak assemblages. Metapelitic sample 830-20 contains a peak assemblage of biotite, garnet, rutile, ilmenite, plagioclase, quartz, sillimanite and melt, and metamafic sample 830-23 has a peak assemblage of garnet, hornblende, biotite, ilmenite, magnetite, plagioclase, K-feldspar and melt. Notably, kyanite, staurolite, and rutile inclusions inside porphyroblastic garnet in sample 830-20 suggest the rock experienced Barrovian-style metamorphism during its prograde

history. Peak *P–T* conditions constrained by these samples are ~8–9 kbar and 780–840°C (Figure 6a,b). Although modelled temperatures appear slightly lower in the migmatitic rocks, the inferred peak pressures overlap with the estimated M2 pressures in the *HT-UHT* samples and are followed by an equivalent post-peak pressure decrease, suggesting both rock systems record the same geologic event.

In sample 830-20, U–Pb results from monazite and Lu–Hf results from coarse-grained (~1 cm) metamorphic garnet yield ages of c. 1150 Ma and c. 1160 Ma, respectively (Figure 7c and 11b). Sample 830-23 comes from the migmatized margin of the mafic rock system that borders the *HT-UHT* rocks. U–Pb titanite results from sample 830-23 yielded an intercept age of 1125 ± 8 Ma (Figure 12).

Zircon U–Pb ages in samples 830-20 and 830-23 can be separated into three populations: an early Paleoproterozoic population at 2600–2200 Ma, a late Paleoproterozoic population at c. 1630 Ma, and a Mesoproterozoic population at 1190–1180 Ma (inset, Figure 9c,d). In the metapelitic sample 830-20, the dominant age population is c. 1630 Ma. Concordant zircon older than c. 1200 Ma are characterized by relatively high HREE contents and a wide range of Th/U (0.01–0.62). In contrast, zircon with $^{207}Pb/^{206}Pb$ ages between 1197 and 1144 Ma have comparatively low HREE concentrations and low Th/U (0.01–0.05). Depleted HREE concentrations are typical of zircon that formed in the presence of garnet (e.g., Hokada & Harley, 2004; Johnson et al., 2021; Rubatto & Hermann, 2003; Whitehouse & Platt, 2003), and low Th/U may indicate coeval growth with a Th-rich mineral(s), such as monazite (e.g., Yakymchuk et al., 2018). The origin of zircons older than c. 1200 Ma is less obvious. Based on their compositions and absence of evidence for polymetamorphism, it is unlikely zircons >1200 Ma are metamorphic in origin. Instead, we tentatively suggest they could be detrital, implying the protolith has a maximum depositional age of ~1630 Ma. Scrimgeour, Close, and Edgoose (2005); Scrimgeour, Kinny, et al. (2005) showed the bulk of the magmatism in the central western Warumpi Province is ~1630 Ma in age, providing a source of age correlative detritus. The array of discordant zircon between 1600 and 1200 Ma likely reflects Pb-loss but may also include some mixing of age domains. In sample 830-23, the dominant age population is c. 1630 Ma and is preserved mainly by oscillatory zoned zircons, most likely derived from the mafic protolith. There is a small population of older grains that are potentially inherited, and a minor population of zircon with ages clustering around c. 1150 Ma. A discordant array of compositions that track towards c. 1150 Ma could be explained by a combination of variable Pb-loss and mixing of domains of different ages within the ablated volume. The youngest zircon ages are consistent with U–Pb results obtained from titanite (Figure 12).

5.3 | Contrasting accessory mineral responses during high-temperature reworking

We interpret the geochronological record preserved in the high-Mg rocks from the Yaya Hills to reflect the formation of a M1 assemblage during the c. 1640–1610 Ma Liebig Orogeny, and the subsequent development of a *HT-UHT* M2 assemblage during the c. 1150 Ma Musgrave Orogeny. In contrast, the migmatized metapelitic and metamafic samples record clear evidence for metamorphism during the Musgrave Orogeny and show no obvious geochronological record for metamorphism at c. 1630 Ma, likely because the protoliths were formed at or subsequent to c. 1630 Ma.

For the metapelitic rocks in this study, the primary differences between migmatized rocks and the domain of *(U)HT* rocks in the Yaya Hills are (1) differing amounts of SiO_2, (2) bulk rock X_{Mg} and (3) aluminosilicates. The *HT-UHT* rocks are comparatively depleted in SiO_2 and have elevated X_{Mg} compositions relative to the surrounding, migmatitic country rocks. Compared to the fertile migmatitic lithologies, the *HT-UHT* rocks appear to have refractory bulk compositions. The reasons for this are beyond the scope of this study. However, we note the formation of refractory bulk compositions derived from sedimentary protoliths can occur in a number of different ways. Previous work has shown that melting and melt loss can create refractory bulk compositions which are commonly characterized by migmatitic-style rocks containing peritectic K-feldspar (e.g., Brown, 2001; Clark et al., 2011; Hand, Mawby, Kinny, & Foden, 1999; Korhonen, Saito, Brown, & Siddoway, 2010; Morrissey et al., 2014; White et al., 2002). A second mechanism is low temperature hydrothermal alteration. The voluminous hydrothermal formation of Mg-Al-rich chlorites (sudoite) commonly occurs in association with unconformity U deposits and is associated with the loss of Si, K, Ca, and Na (e.g., Billault et al., 2002; Nutt, 1989; Percival & Kodama, 1989), resulting in rock compositions that resist melting despite being significantly hydrous. A third mechanism is the formation of Mg-rich clay deposits in lacustrine saline-alkaline semi-arid environments (Herranz & Pozo, 2018; Pozo & Calvo, 2018). Irrespective of the mechanism by which the refractory bulk compositions represented by samples 830-6 and 830-7 formed, the direct ramification is the resistance of these samples to melting during M2, despite the high

temperatures they experienced. Their resistance to melting is most obviously evidenced by the non-migmatitic nature of the rocks.

It is well recognized that melting enhances the responsiveness of accessory minerals to metamorphism (e.g., Johnson et al., 2015; Kelsey et al., 2008; Kelsey & Powell, 2010; Rubatto et al., 2001; Yakymchuk & Brown, 2014). Previous work has demonstrated the inhibited (re)crystallization of chronometers such as zircon and monazite during granulite facies metamorphism when rocks remain below the solidus (e.g., Högdahl et al., 2012; Korhonen et al., 2012; McFarlane et al., 2006; Morrissey et al., 2016; Phillips et al., 2007; Tenczer et al., 2006; White & Powell, 2002; Yakymchuk & Brown, 2014). Indeed, it is often noted that in polymetamorphic terranes only the first metamorphic event is well-recorded, and that subsequent events usually only involve partial re-equilibration (e.g., Franceschelli et al., 1998; Morrissey et al., 2016; Rickers et al., 2001; Tenczer et al., 2006; Zeck & Whitehouse, 2002). This phenomenon appears to have only partially manifested in the Yaya Hills region of the Warumpi Province, where in the polymetamorphic *HT-UHT* rocks, U–Pb geochronology from both zircon and monazite almost exclusively records the Liebig Orogeny, despite M2 metamorphism at c. 1150 Ma reaching temperatures as high as 900°C. In contrast, the migmatitic samples that seemingly lack clear evidence for Leibig-aged mineral assemblages record unambiguous Musgrave-aged metamorphism.

Previous explanations for the preferential preservation of some events over others in polymetamorphic terranes have discussed both duration and localized fluid availability/hydration as potential factors (e.g., Korhonen et al., 2012; Lister et al., 2001; Phillips et al., 2007; Stuewe & Ehlers, 1996; Tenczer et al., 2006). We do not speculate on the relative durations of the Liebig Orogeny and Musgrave Orogeny in this study; however, we suggest the availability of H_2O and suitable compositional fertility (e.g., Si and alkali elements) exerts an influential role on their respective geochronological fingerprints. Melting is heavily reliant on the presence of H_2O, whether as a free phase or within hydrous minerals such as muscovite or biotite (e.g., Campbell & Taylor, 1983; Fyfe, 1976; Johannes & Holtz, 1996; Schwindinger et al., 2018; Sola et al., 2017; Weinberg & Hasalová, 2015). For chronometers such as zircon and monazite, which often depend on melting to facilitate their crystallization, their preserved geochronologic records may therefore be heavily dictated by the availability of H_2O (e.g., Korhonen et al., 2012; Morrissey et al., 2016; Vielzeuf et al., 1990; White & Powell, 2002). We suggest that rocks recording M2 assemblages were compositionally fertile in contrast to refractory rocks with well-preserved M1 assemblages, leading to contrasting accessory mineral records.

Of note, the age distribution obtained from zircon and monazite in this study is based on LA–ICP–MS analysis of zircon grains that exceed ~30 μm in size, and monazite grains of >20 μm. In both samples 830-6 and 830-7, M2 reaction volumes commonly contain extremely abundant fine grained (<5 μm) populations of monazite and zircon (Appendix SB). Feasibly, there may have been a more overt accessory mineral response to c. 1150 Ma *(U)HT* M2 metamorphism recorded in grains that were too small to analyse. The abundance of these small monazite and zircon grains may have also impacted the ability of larger grains to recrystallise and record M2. Previous work has demonstrated the dependence of accessory mineral (re)crystallization on low temperatures and system saturation in REEs, as well as Zr and/or phosphates, depending on the mineral(s) being crystallized (Johnson et al., 2015; Kelsey et al., 2008; Kelsey & Powell, 2010; Rubatto et al., 2001; Yakymchuk et al., 2017; Yakymchuk & Brown, 2014). If minor amounts of melt were generated in the small-scale reactive M2 domains, perhaps the fine-grained monazite and zircon grains were the sole accessory mineral chronometers to (re)crystallize during the c. 1150 Ma Musgrave Orogeny. Conceivably, grains coarse enough to be analysed for geochronology remained largely unaffected by the presence of the low melt abundances predicted to occur in the M2 reaction domains.

The apparent limited response of zircon and monazite to *(U)HT* reworking has implications for how we decipher polymetamorphic records in high temperature terranes. Previously, LA–ICP–MS accessory mineral geochronology and trace element chemistry has been among the most efficient and utilized methods for constraining the timing of metamorphic events. However, the present study illuminates the advantage of directly dating thermobarometrically important minerals, such as garnet. Similarly, Thiessen et al. (2019) demonstrated accessory minerals in high grade rocks in the Rae Craton, Canada were resistant to high-temperature reworking. The ability to obtain Lu–Hf age constraints on *HT-UHT* garnet illuminates firstly, the polymetamorphic record preserved within these rocks, and secondly, the inhibited response of zircon and monazite in rocks that did not undergo significant partial melting (Thiessen et al., 2019). Without Lu–Hf dating of garnet or analysis of the surrounding migmatized rocks, it would be understandable—and logical—to tie the *HT-UHT* 8–10 kbar M2 metamorphism recorded in samples 830-6 and 830-7 to the M1 Liebig Orogeny which actually occurred ~500 Myr prior. Indeed, this has been the prevailing interpretation in all previous work focused on the

Warumpi Province (e.g., Ahmad & Munson, 2013; Scrimgeour, Close, & Edgoose, 2005), with the recorded pressures used to underpin models for continental collision in central Australia. In contrast, we suggest Liebig-aged metamorphism is low-pressure, predominantly localized around magmatic intrusions, and a precursor to the more pervasive, *(U)HT* Musgrave Orogeny.

6 | CONCLUSION

Multi-method geochronology, geochemistry, and mineral equilibria forward modelling are combined to interrogate the polymetamorphic history of the Warumpi Province in central Australia. Results from this study support the following conclusions:

1. Polymetamorphic terranes that create refractory bulk compositions in their early history may be less susceptible to melting, and therefore resistant to (re)crystallizing accessory mineral chronometers during later episodes of metamorphism. The inhibited response of these accessory minerals can cause geochronology and *P–T* constraints to become decoupled, contributing ambiguity when attempting to decipher the tectonometamorphic history of polymetamorphic rocks.
2. Lu–Hf geochronology of garnet evidences *(U)HT* metamorphism in the Warumpi Province actually occurred during the Musgrave Orogeny, contrary to previous work that relied on zircon and monazite U–Pb geochronology and assigned *(U)HT* conditions to the c. 1640 Ma Liebig Orogeny. As indicated by relict andalusite and orthopyroxene–cordierite-bearing assemblages, the Liebig Orogeny was likely a low pressure event with a high thermal gradient. We suggest that it may have involved the intrusion of mafic and felsic intrusions around the Warumpi Province, including the gabbroic body that today neighbours the Yaya Hills.
3. In polymetamorphic terranes, conventional geochronology using accessory minerals such as zircon and monazite should be supplemented by geochronology that directly dates the peak assemblage, an example being Lu–Hf geochronology of garnet.

ACKNOWLEDGEMENTS

The authors acknowledge and pay their respects to the Luritja people, the Traditional Custodians of the land on which the samples defining this study were collected. This research was conducted at the University of Adelaide. The authors would like to thank Aoife McFadden, Sarah Gilbert and Benjamin Wade at Adelaide Microscopy for their assistance with data collection and processing. Additionally, they would like to acknowledge Curtin University for their assistance with separating zircons from samples 830-6 and 830-7. Samantha March acknowledges financial support from the Robert Francis Thyer Award, Playford Trust PhD Scholarship, Australian Institute of Geoscientists Student Bursary, and the Geological Society of Australia Endowment Fund. This research is supported by Australian Research Council grant DP220103037. Laura Morrissey is supported by an Australian Research Council DECRA Fellowship, DE210101126. David Kelsey publishes with the permission of the Executive Director, Geological Survey of Western Australia. Matthijs Smit and Chris Yakymchuk are thanked for the time and insight given to constructing thoughtful reviews that greatly improved the manuscript. Chunjing Wei and Richard White are acknowledged for their editorial handling. Open access publishing facilitated by The University of Adelaide, as part of the Wiley - The University of Adelaide agreement via the Council of Australian University Librarians.

DATA AVAILABILITY STATEMENT

The data that supports the findings of this study are available in the supplementary material of this article

REFERENCES

Ahmad, M., & Munson, T. J. (2013). *Geology and mineral resources of the Northern Territory*. Northern Territory Geological Survey, Special Publication 5.

Ahmad, M., & Scrimgeour, I. R. (2006). *Geological map of the Northern Territory* (Vol. 1). Northern Territory Geological Survey, *2 500 000 scale*

Asami, M., Suzuki, K., & Grew, E. S. (2002). Chemical Th–U–total Pb dating by electron microprobe analysis of monazite, xenotime and zircon from the Archean Napier complex, East Antarctica: Evidence for ultra-high-temperature metamorphism at 2400 ma. *Precambrian Research*, *114*(3–4), 249–275. https://doi.org/10.1016/S0301-9268(01)00228-5

Ashworth, J. R., Reverdatto, V., Kolobov, V., Lepetyukha, V., Sheplev, V., & Bryxina, N. (1998). Textures of diffusion-controlled reaction in contact-metamorphosed mg-rich granulite, Kokchetav area, Kazakhstan. *Mineralogical Magazine*, *62*(2), 213–224. https://doi.org/10.1180/002646198547585

Ashworth, J. R., Reverdatto, V. V., Kolobov, V. YU., Lepetyukha, V. V., Sheplev, V. S., & Bryxina, N. A., (1998). Textures of diffusion-controlled reaction in contact-metamorphosed Mg-rich granulite, Kokchetav area, Kazakhstan. *Mineralogical Magazine*, *62*(2), 213–224. https://doi.org/10.1180/002646198547585

Biermeier, C., Stüwe, K., Foster, D. A., & Finger, F. (2003). Thermal evolution of the Redbank thrust system, Central Australia; geochronological and phase-equilibrium constraints. *Tectonics*, *22*(1), 1002. https://doi.org/10.1029/2001TC901033

Billault, V., Beaufort, D., Patrier, P., & Petit, S. (2002). Crystal chemistry of Fe-sudoites from uranium deposits in the

Athabasca Basin (Saskatchewan, Canada). *Clays and Clay Minerals*, *50*(1), 70–81. https://doi.org/10.1346/000986002761002847

Black, L. P., & Shaw, R. D. (1995). An assessment, based on U-Pb zircon data, of Rb-Sr dating in the Arunta inlier, Central Australia. *Precambrian Research*, *71*(1–4), 3–15. https://doi.org/10.1016/0301-9268(94)00053-T

Bloch, E., & Ganguly, J. (2015). Lu-Hf geochronology of garnet II: Numerical simulations of the development of garnet-whole-rock Lu-Hf isochrons and a new method for constraining the thermal history of metamorphic rocks. *Contributions to Mineralogy and Petrology*, *169*(2), 14. https://doi.org/10.1007/s00410-015-1115-x

Bloch, E., Ganguly, J., Hervig, R., & Cheng, W. (2015). 176Lu–176Hf geochronology of garnet I: Experimental determination of the diffusion kinetics of Lu3+ and Hf4+ in garnet, closure temperatures and geochronological implications. *Contributions to Mineralogy and Petrology*, *169*(2), 12. https://doi.org/10.1007/s00410-015-1109-8

Bloch, E., Jollands, M., Devoir, A., Bouvier, A., Ibañez-Mejia, M., & Baumgartner, L. (2020). Multispecies diffusion of yttrium, rare earth elements and hafnium in garnet. *Journal of Petrology*, *61*(7). https://doi.org/10.1093/petrology/egaa055

Briqueu, L., Bougalt, H., & Joron, J. L. (1984). Quantification of Nb, ta, Ti and V anomalies in magmas associated with subduction zones: Petrogenetic implications. *Earth and Planetary Science Letters*, *68*(2), 297–308. https://doi.org/10.1016/0012-821X(84)90161-4

Brown, M., (2001). Orogeny, migmatites and leucogranites: A review. *Journal of Earth System Science*, *110*(4), 313–336. https://doi.org/10.1007/bf02702898

Brown, M., & Korhonen, F. J. (2009). *Some remarks on melting and extreme metamorphism of crustal rocks*. Springer. https://doi.org/10.1007/978-1-4419-0346-4_4

Campbell, I. H., & Taylor, S. R. (1983). No water, no granites—Nooceans, no continents. *Geophysical Research Letters*, *10*(11), 1061–1064. https://doi.org/10.1029/GL010i011p01061

Carlson, W. D. (2010). Dependence of reaction kinetics on H2O activity as inferred from rates of intergranular diffusion of aluminium. *Journal of Metamorphic Geology*, *28*(7), 735–752. https://doi.org/10.1111/j.1525-1314.2010.00886.x

Cherniak, D. J., & Watson, E. B. (2001). Pb diffusion in zircon. *Chemical Geology*, *172*(1–2), 5–24. https://doi.org/10.1016/S0009-2541(00)00233-3

Cherniak, D. J., Watson, E. B., Grove, M., & Harrison, T. M. (2004). Pb diffusion in monazite: A combined RBS/SIMS study. *Geochimica et Cosmochimica Acta*, *68*(4), 829–840. https://doi.org/10.1016/j.gca.2003.07.012

Claoué-Long, J. C., & Hoatson, D. M. (2005). Proterozoic mafic–ultramafic intrusions in the Arunta region, Central Australia. Part 2: Event chronology and regional correlations. *Precambrian Research*, *142*, 134–258. https://doi.org/10.1016/j.precamres.2005.08.006

Clark, C., Fitzsimons, I. C. W., Healy, D., & Harley, S. L. (2011). How does the continental crust get really hot? *Elements*, *7*(4), 235–240. https://doi.org/10.2113/gselements.7.4.235

Close, D. F., Scrimgeour, I. R., Edgoose, C., Wingate, M. T. D., & Selway, K. (2005). Late Palaeoproterozoic oblique accretion of a 1690–1660 ma magmatic arc onto the north Australian craton. *Geological Society of Australia, Abstracts*, *81*, 36.

Collins, W. J., & Shaw, R. D. (1995). Geochronological constraints on orogenic events in the Arunta inlier: A review. *Precambrian Research*, *71*(1–4), 315–346. https://doi.org/10.1016/0301-9268(94)00067-2

Cutts, K., Hand, M., & Kelsey, D. E. (2011). Evidence for early Mesoproterozoic (ca. 1590 ma) ultrahigh-temperature metamorphism in southern Australia. *Lithos*, *124*(1–2), 1–16. https://doi.org/10.1016/j.lithos.2010.10.014

Diener, J. F. A., White, R. W., & Powell, R. (2008). Granulite facies metamorphism and subsolidus fluid-absent reworking, Strangways range, Arunta block, Central Australia. *Journal of Metamorphic Geology*, *26*(6), 603–622. https://doi.org/10.1111/j.1525-1314.2008.00782.x

Droop, G. T. R. (1987). A general equation for estimating Fe3+ concentrations in ferromagnesian silicates and oxides from microprobe analyses, using stoichiometric criteria. *Mineralogical Society*, *51*(361), 431–435. https://doi.org/10.1180/minmag.1987.051.361.10

Elburg, M. A., Bons, P. D., Foden, J., & Brugger, J. (2003). A newly defined late Ordovician magmatic–thermal event in the Mt Painter Province, northern Flinders ranges, South Australia. *Australian Journal of Earth Sciences*, *50*(4), 611–631. https://doi.org/10.1046/j.1440-0952.2003.01016.x

Franceschelli, M., Eltrudis, A., Memmi, I., Palmeri, R., & Carcangiu, G. (1998). Multi-stage metamorphic re-equilibration in eclogitic rocks from the Hercynian basement of NE Sardinia (Italy). *Mineralogy and Petrology*, *62*, 167–193. https://doi.org/10.1007/BF01178028

Fraser, G., Ellis, D. J., & Eggins, S. (1997). Zirconium abundance in granulite-facies minerals, with implications for zircon geochronology in high-grade rocks. *Geology*, *25*(7), 607–610. https://doi.org/10.1130/0091-7613(1997)025<0607:ZAIGFM>2.3.CO;2

Fyfe, W. S. (1976). Discussion on natural strain and geological structure—Chemical aspects of rock deformation. *Philosophical Transactions of the Royal Society of London*, *283*(1312), 221–228. https://doi.org/10.1098/rsta.1976.0080

Green, D. H., White, R. W., Diener, J. F. A., Powell, R., Holland, T. J., & Palin, R. M. (2016). Activity–composition relations for the calculation of partial melting equilibria in metabasic rocks. *Journal of Metamorphic Geology*, *34*(9), 845–869. https://doi.org/10.1111/jmg.12211

Guevara, V. E., & Caddick, M. J. (2016). Shooting at a moving target: Phase equilibria modelling of high-temperature metamorphism. *Journal of Metamorphic Geology*, *34*(3), 209–235. https://doi.org/10.1111/jmg.12179

Guilmette, C., Smit, M. A., Van Hinsbergen, D. D. J., Gürer, D., Corfu, F., Charette, B., Maffione, M., Rabeau, O., & Savard, D. (2018). Forced subduction initiation recorded in the sole and crust of the Semail ophiolite of Oman. *Nature Geoscience*, *11*, 688–695. https://doi.org/10.1038/s41561-018-0209-2

Hand, M., Mawby, J. O., Kinny, P., & Foden, J., (1999). U–Pb ages from the Harts Range, central Australia: evidence for early Ordovician extension and constraints on Carboniferous metamorphism. *Journal of the Geological Society*, *156*(4), 715–730. https://doi.org/10.1144/gsjgs.156.4.0715

Hellstrom, J., Paton, C., Woodhead, J., & Hergt, J. (2008). Iolite: Software for spatially resolved LA-(quad and MC) ICPMS analysis. *Mineralogical Association of Canada Short Course Series*, *40*, 343–348.

Herranz, J. E., & Pozo, M. (2018). Authigenic mg-clay minerals formation in Lake margin deposits (the Cerro de los Batallones Madrid Basin, Spain). *Minerals*, *8*(418), 418. https://doi.org/10.3390/min8100418

Högdahl, K., Majka, J., Sjöström, H., Persson Nilsson, K., Claesson, S., & Konečný, P. (2012). Reactive monazite and robust zircon growth in diatexites and leucogranites from a hot, slowly cooled orogen: Implications for the Palaeoproterozoic tectonic evolution of the central Fennoscandian shield, Sweden. *Contributions to Mineralogy and Petrology*, *163*, 167–188. https://doi.org/10.1007/s00410-011-0664-x

Hokada, T., & Harley, S. L. (2004). Zircon growth in UHT leucosome: Constraints from zircon-garnet rare earth elements (REE) relations in Napier complex, East Antarctica. *Journal of Mineralogical and Petrological Sciences*, *99*, 180–190. https://doi.org/10.2465/jmps.99.180

Holland, T. J., & Powell, R. (2003). Activity–composition relations for phases in petrological calculations: An asymmetric multicomponent formulation. *Contributions to Mineralogy and Petrology*, *145*, 492–501. https://doi.org/10.1007/s00410-003-0464-z

Holland, T. J., & Powell, R. (2011). An improved and extended internally consistent thermodynamic dataset for phases of petrological interest, involving a new equation of state for solids. *Journal of Metamorphic Geology*, *29*(3), 333–383. https://doi.org/10.1111/j.1525-1314.2010.00923.x

Hollister, L. (1966). Garnet zoning: An interpretation based on the Rayleigh fractionation model. *Science*, *154*(3757), 1647–1651. https://doi.org/10.1126/science.154.3757.1647

Jackson, S. E., Pearson, N. J., Griffin, W. L., & Belousova, E. A. (2004). The application of laser ablation-inductively coupled plasma-mass spectrometry to in situ U–Pb zircon geochronology. *Chemical Geology*, *211*(1), 47–69. https://doi.org/10.1016/j.chemgeo.2004.06.017

Jennings, E. S., & Holland, T. J. (2015). A simple thermodynamic model for melting of peridotite in the system NCFMASOCr. *Journal of Petrology*, *56*(5), 869–892. https://doi.org/10.1093/petrology/egv020

Johannes, W., & Holtz, F. (1996). *Petrogenesis and experimentalpetrology of granitic rocks*. Springer. https://doi.org/10.1007/978-3-642-61049-3

Johnson, T. E., Clark, C., Taylor, R. J. M., Santosh, M., & Collins, A. S. (2015). Prograde and retrograde growth of monazite in migmatites: An example from the Nagercoil block, southern India. *Geoscience Frontiers*, *6*, 373–387. https://doi.org/10.1016/j.gsf.2014.12.003

Johnson, T., Vervoort, J. D., Ramsey, M., Aleinikoff, J., & Southworth, S. (2018). Constraints on the timing and duration of orogenic events by combined Lu–Hf and Sm–Nd geochronology: An example from the Grenville orogeny. *Earth and Planetary Science Letters*, *501*, 152–164. https://doi.org/10.1016/j.epsl.2018.08.030

Johnson, T., Yakymchuk, C., & Brown, M. (2021). Crustal melting and suprasolidus phase equilibria: From first principles to the state-of-the-art. *Earth-Science Reviews*, *221*, 103778. https://doi.org/10.1016/j.earscirev.2021.103778

Kelly, E. D., Carlson, W. D., & Connelly, J. N. (2011). Implications of garnet resorption for the Lu–Hf garnet geochronometer: An example from the contact aureole of the Makhavinekh Lake pluton, Labrador. *Journal of Metamorphic Geology*, *29*(8), 901–916. https://doi.org/10.1111/j.1525-1314.2011.00946.x

Kelsey, D. E., Clark, C., & Hand, M. (2008). Thermobarometric modelling of zircon and monazite growth in melt-bearing systems: Examples using model metapelitic and metapsammitic granulites. *Journal of Metamorphic Geology*, *26*(2), 199–212. https://doi.org/10.1111/j.1525-1314.2007.00757.x

Kelsey, D. E., & Powell, R. (2010). Progress in linking accessory mineral growth and breakdown to major mineral evolution in metamorphic rocks: A thermodynamic approach in the Na2O-CaO-K2O-FeO-MgO-Al2O3-SiO2-H2O-TiO2-ZrO2 system. *Journal of Metamorphic Geology*, *29*(1), 151–166. https://doi.org/10.1111/j.1525-1314.2010.00910.x

Kohn, M. J. (2009). Models of garnet differential geochronology. *Geochimica et Cosmochimica Acta*, *73*(1), 170–182. https://doi.org/10.1016/j.gca.2008.10.004

Korhonen, F. J., Brown, M., Grove, M., Siddoway, C. S., Baxter, E. F., & Inglis, J. D. (2012). Separating metamorphic events in the Fosdick migmatite-granite complex, West Antarctica. *Journal of Metamorphic Geology*, *2012*(30), 165–191. https://doi.org/10.1111/j.1525-1314.2011.00961.x 2011 Blackwell Publishing Ltd165

Korhonen, F. J., Clark, C., Brown, M., Bhattacharya, S., & Taylor, R. (2013). How long-lived is ultrahigh temperature (UHT) metamorphism? Constraints from zircon and monazite geochronology in the eastern Ghats orogenic belt, India. *Precambrian Research*, *234*, 322–350. https://doi.org/10.1016/j.precamres.2012.12.001

Korhonen, F. J., Saito, S., Brown, M., & Siddoway, C. S., (2010). Modeling multiple melt loss events in the evolution of an active continental margin. *Lithos*, *116*(3–4), 230–248. https://doi.org/10.1016/j.lithos.2009.09.004

Lapen, T. J., Johnson, C. M., Baumgartner, L., Mahlen, N. J., Beard, B. L., & Amato, J. (2003). Burial rates during prograde metamorphism of an ultra-high-pressure terrane: An example from Lago di Cignana, western Alps, Italy. *Earth and Planetary Science Letters*, *215*(1–2), 57–72. https://doi.org/10.1016/S0012-821X(03)00455-2

Lee, J. K. W., Williams, I. S., & Ellis, D. J. (1997). Pb, U and Th diffusion in natural zircon. *Nature*, *390*, 159–162. https://doi.org/10.1038/36554

Lister, G. S., Forster, M. A., & Rawling, T. J. (2001). Episodicity during orogenesis. *Geological Society, London, Special Publications*, *184*, 89–113. https://doi.org/10.1144/GSL.SP.2001.184.01.06

Maidment, D. (2005). *Palaeozoic high-grade metamorphism within the Centralian Superbasin, harts range region, Central Australia*. Australian National University. (unpublished)

McFarlane, C. R. M., Carlson, W. D., & Connelly, J. N. (2003). Prograde, peak, and retrograde P–T paths from aluminium in orthopyroxene: High-temperature contact metamorphism in the aureole of the Makhavinekh Lake pluton, Nain plutonic suite, Labrador. *Journal of Metamorphic Geology*, *21*(5), 405–423. https://doi.org/10.1046/j.1525-1314.2003.00446.x

McFarlane, C. R. M., Connelly, J. N., & Carlson, W. D. (2006). Contrasting response of monazite and zircon to a high-T thermal

overprint. *Lithos*, *88*(1–4), 135–149. https://doi.org/10.1016/j.lithos.2005.08.008

McFarlane, C. R. M., & Harrison, T. M. (2006). Pb-diffusion in monazite: Constraints from a high-T contact aureole setting. *Earth and Planetary Science Letters*, *250*(1–2), 376–384. https://doi.org/10.1016/j.epsl.2006.06.050

Morrissey, L. J., Hand, M., Kelsey, D. E., & Wade, B. (2016). Cambrian high-temperature reworking of the Rayner–Eastern Ghats terrane: Constraints from the northern Prince Charles mountains region, East Antarctica. *Journal of Petrology*, *57*(1), 53–92. https://doi.org/10.1093/petrology/egv082

Morrissey, L. J., Hand, M., Raimondo, T., & Kelsey, D. E. (2014). Long-lived high-T, low-P granulite facies metamorphism in the Arunta region, Central Australia. *Journal of Metamorphic Geology*, *32*(1), 25–47. https://doi.org/10.1111/jmg.12056

Morrissey, L. J., Payne, J. L., Kelsey, D. E., & Hand, M. (2011). Grenvillian-aged reworking in the north Australian craton, Central Australia: Constraints from geochronology and modelled phase equilibria. *Precambrian Research*, *191*(3–4), 141–165. https://doi.org/10.1016/j.precamres.2011.09.010

Nabelek, P. I., Hofmeister, A. M., & Whittington, A. G. (2012). The influence of temperature-dependent thermal diffusivity on the conductive cooling rates of plutons and temperature-time paths in contact aureoles. *Earth and Planetary Science Letters*, *317-318*, 157–164. https://doi.org/10.1016/j.epsl.2011.11.009

Nebel, O., Morel, M. L., & Vroon, P. Z. (2009). Isotope dilution determinations of Lu, Hf, Zr, ta and W, and Hf isotope compositions of NIST SRM 610 and 612 glass wafers: Geostandards and Geoanalytical research. *Geostandards and Geoanalytical Research*, *33*(4), 487–499. https://doi.org/10.1111/j.1751-908X.2009.00032.x

Norris, A., & Danyushevsky, L. (2018). *Towards estimating the complete uncertainty budget of quantified results measured by LA-ICP-MS*. Goldschmidt.

Nutt, C. J. (1989). Chloritization and associated alteration at the Jabiluka unconformity-type uranium deposit, Northern Territory, Australia. *Canadian Mineralogist*, *27*, 41–58.

Paton, C., Hellstrom, J., Paul, B., Woodhead, J., & Hergt, J. (2011). Iolite: Freeware for the visualisation and processing of mass spectrometric data. *Journal of Analytical Atomic Spectrometry*, *26*(12), 2508–2518. https://doi.org/10.1039/c1ja10172b

Payne, J. L., Hand, M., Barovich, K., & Wade, B. (2008). Temporal constraints on the timing of high-grade metamorphism in the northern Gawler craton: Implications for assembly of the Australian Proterozoic. *Australian Journal of Earth Sciences*, *55*(5), 623–640. https://doi.org/10.1080/08120090801982595

Pearce, N. J. G., Perkins, W. T., Westgate, J. A., Gorton, M. P., Jackson, S. E., Neal, C. R., & Chenery, S. P. (2007). A compilation of new and published major and trace element data for NIST SRM 610 and NIST SRM 612 glass reference material. *Geostandards Newsletter*, *21*(1), 115–144. https://doi.org/10.1111/j.1751-908X.1997.tb00538.x

Percival, J. B., & Kodama, H. (1989). Sudoite from cigar Lake, Saskatchewan. *Canadian Mineralogist*, *27*(4), 633–641.

Phillips, G., White, R. W., & Wilson, C. J. L. (2007). On the roles of deformation and fluid during rejuvenation of a polymetamorphic terrane: Inferences on the geodynamic evolution of the Ruker Province, East Antarctica. *Journal of Metamorphic Geology*, *25*(8), 855–871. https://doi.org/10.1111/j.1525-1314.2007.00732.x

Pozo, M., & Calvo, J. (2018). An overview of Authigenic Magnesian clays. *Minerals*, *8*(520), 520. https://doi.org/10.3390/min8110520

Rasmussen, B., Muhling, J., Fletcher, R., & Wingate, M. T. D. (2006). In situ SHRIMP U–Pb dating of monazite integratedwith petrology and textures: Does bulk composition control whether monazite forms in low-ca pelitic rocks during amphibolite facies metamorphism. *Geochimica et Cosmochimica Acta*, *70*, 3040–3058. https://doi.org/10.1016/j.gca.2006.03.025

Rickers, K., Raith, M., & Dasgupta, S. (2001). Multistage reaction textures in xenolithic high-MgAl granulites at Anakapalle, eastern Ghats Belt, India: Examples of contact polymetamorphism and infiltration-driven metasomatism. *Journal of Metamorphic Geology*, *19*(5), 563–582. https://doi.org/10.1046/j.0263-4929.2001.00329.x

Romer, R. L., & Smeds, S. (1996). U-Pb columbite ages of pegmatites from Sveconorwegian terranes in southwestern Sweden. *Precambrian Research*, *76*(1–2), 15–30. https://doi.org/10.1016/0301-9268(95)00023-2

Rubatto, D. (2002). Zircon trace element geochemistry: Partitioning with garnet and the link between U–Pb ages and metamorphism. *Chemical Geology*, *184*(1–2), 123–138. https://doi.org/10.1016/S0009-2541(01)00355-2

Rubatto, D., & Hermann, J. (2003). Zircon formation during fluid circulation in eclogites (Monviso, Western Alps): Implications for Zr and Hf budget in subduction zones. *Geochimica et Cosmochimica Acta*, *67*(12), 2173–2187. https://doi.org/10.1016/S0016-7037(02)01321-2

Rubatto, D., Williams, I. S., & Buick, I. S. (2001). Zircon and monazite response to prograde metamorphism in the Reynolds range, Central Australia. *Contributions to Mineralogy and Petrology*, *140*, 458–468. https://doi.org/10.1007/PL00007673

Sajeev, K., Williams, I. S., & Osanai, Y. (2010). Sensitive high-resolution ion microprobe U-Pb dating of prograde and retrograde ultrahigh-temperature metamorphism as exemplified by Sri Lankan granulites. *Geology*, *38*(11), 971–974. https://doi.org/10.1130/G31251.1

Santosh, M., Collins, A. S., Tamashiro, I., Koshimoto, S., Tsutsumi, Y., & Yokoyama, K. (2006). The timing of ultrahigh-temperature metamorphism in southern India: U–Th–Pb electron microprobe ages from zircon and monazite in sapphirine-bearing granulites. *Gondwana Research*, *10*(1–2), 128–155. https://doi.org/10.1016/j.gr.2005.12.005

Scherer, E., Münker, C., & Mezger, K. (2001). Calibration of the lutetium-hafnium clock. *Science*, *293*(5530), 683–687. https://doi.org/10.1126/science.1061372

Scherer, E. E., Cameron, K. L., & Blichert-Toft, J., (2000). Lu–hf garnet geochronology: closure temperature relative to the Sm–Nd system and the effects of trace mineral inclusions. *Geochimica et Cosmochimica Acta*, *64*(19), 3413–3432. https://doi.org/10.1016/0301-9268(94)00055-V

Schmitz, M. D., & Bowring, S. A. (2003). Ultrahigh-temperature metamorphism in the lower crust during Neoarchean Ventersdorp rifting and magmatism, Kaapvaal craton, southern Africa. *GSA Bulletin*, *115*(5), 533–548. https://doi.org/10.1130/0016-7606(2003)115<0533:UMITLC>2.0.CO;2

Schorn, S., Diener, J. F. A., Powell, R., & Stüwe, K. (2018). Thermal buffering in the orogenic crust. *Geology*, *46*(7), 643–646. https://doi.org/10.1130/G40246.1

Schwindinger, M., Weinberg, R. F., & Clos, F. (2018). Wet or dry? The difficulty of identifying the presence of water during crustal melting. *Journal of Metamorphic Geology*, *37*(3), 339–358. https://doi.org/10.1111/jmg.12465

Scrimgeour, I. R. (2013). Chapter 13: Warumpi Province. In M. Ahmad & T. J. Munson (Eds.), (compilers)'*Geology and mineral resources of the Northern Territory'. Northern Territory geological survey, special publication*, (Vol. 5).

Scrimgeour, I. R., Close, D. F., & Edgoose, C. (2005). Mount Liebig Northern Territory. 1 250 000 Geological Map Series Explanatory Notes, SF 52–16. In *Northern Territory Geological Survey*.

Scrimgeour, I. R., Kinny, P. D., Close, D. F., & Edgoose, C. J. (2005). High-T granulites and polymetamorphism in the southern Arunta region Central Australia: Evidence for a 1. 64 Ga accretional event. *Precambrian Research*, *142*, 1–27. https://doi.org/10.1016/j.precamres.2005.08.005

Selway, K., Heinson, G., & Hand, M. (2006). Electrical evidence of continental accretion: Steeply-dipping crustal-scale conductivity contrast. *Geophysical Research Letters*, *33*(6). https://doi.org/10.1029/2005GL025328

Shaw, R. D., Zeitler, P. K., Mcdougall, I., & Tingate, P. R. (1992). The Paleozoic history of an unusual intracratonic thrust belt in Central Australia based on 40Ar–39Ar, K–Ar and fission-track dating. *Journal of the Geological Society*, *149*, 937–954. https://doi.org/10.1144/gsjgs.149.6.0937

Simpson, A., Gilbert, S. E., Tamblyn, R., Hand, M., Spandler, C., Gillespie, J., Nixon, A., & Glorie, S. (2021). In-situ Lu–Hf geochronology of garnet, apatite and xenotime by LA ICP MS/MS. *Chemical Geology*, *577*(1–2), 120299. https://doi.org/10.1016/j.chemgeo.2021.120299

Skora, S., Baumgartner, L., Mahlen, N. J., Johnson, C. M., Pilet, S., & Hellebrand, E. (2006). Diffusion-limited REE uptake by eclogite garnets and its consequences for Lu–Hf and Sm–Nd geochronology. *Contributions to Mineralogy and Petrology*, *152*, 703–720. https://doi.org/10.1007/s00410-006-0128-x

Sláma, J., Košler, J., Condon, D. J., Crowley, J. L., Gerdes, A., Hanchar, J. M., Hortswood, M. S. A., Morris, G. A., Nasdala, L., Norberg, N., Schaltegger, U., Schoene, B., Turbett, M. N., & Whitehouse, M. J. (2008). Plešovice zircon—A new natural reference material for U–Pb and Hf isotopic microanalysis. *Chemical Geology*, *249*(1–2), 1–35. https://doi.org/10.1016/j.chemgeo.2007.11.005

Smit, M. A., Scherer, E., & Mezger, K. (2013). Lu–Hf and Sm–Nd garnet geochronology: Chronometric closure and implications for dating petrological processes. *Earth and Planetary Science Letters*, *381*, 222–233. https://doi.org/10.1016/j.epsl.2013.08.046

Söderlund, U., Patchett, P. J., Vervoort, J. D., & Isachsen, C. E. (2004). The 176Lu decay constant determined by Lu–Hf and U–Pb isotope systematics of Precambrian mafic intrusions. *Earth and Planetary Science Letters*, *219*(3–4), 311–324. https://doi.org/10.1016/S0012-821X(04)00012-3

Sola, A. M., Hasalová, P., Weinberg, R. F., Suzaño, N. O., Becchio, R. A., Hongn, F. D., & Botelho, N. (2017). Low-P melting of metapelitic rocks and the role of H2O: Insights from phase equilibria modelling. *Journal of Metamorphic Geology*, *35*(9), 1131–1159. https://doi.org/10.1111/jmg.12279

Spandler, C., Hammerli, J., Sha, P., Hilbert-Wolf, H., Hu, Y., Roberts, E., & Schmitz, M. (2016). MKED1: A new titanite standard for in situ analysis of Sm–Nd isotopes and U–Pb geochronology. *Chemical Geology*, *425*, 110–126. https://doi.org/10.1016/j.chemgeo.2016.01.002

Stuewe, K., & Ehlers, K. (1996). The qualitative zoning record of minerals. A method for determining the duration of metamorphic events? *Mineralogy and Petrology*, *56*, 171–184. https://doi.org/10.1007/BF01162602

Stüwe, K. (1995). Thermal buffering effects at the solidus. Implications for the equilibration of partially melted metamorphic rocks. *Tectonophysics*, *248*(1–2), 39–51. https://doi.org/10.1016/0040-1951(94)00282-E

Tenczer, V., Powell, R., & Stuewe, K. (2006). Evolution of H2O content in a polymetamorphic terrane: The Plattengneiss shear zone (Koralpe, Austria). *Journal of Metamorphic Geology*, *24*(4), 281–295. https://doi.org/10.1111/j.1525-1314.2006.00637.x

Thiessen, E., Gibson, H., Regis, D., Pehrsson, S., Cutts, J., & Smit, M. (2019). High-grade metamorphism flying under the radar of accessory minerals. *Geology*, *47*(6), 568–572. https://doi.org/10.1130/G45979.1

Tucker, N. M., Hand, M., Kelsey, D. E., & Dutch, R. A. (2015). A duality of timescales: Short-lived ultrahigh temperature metamorphism preserving a long-lived monazite growth history in the Grenvillian Musgrave–Albany–Fraser Orogen. *Precambrian Research*, *264*, 204–234. https://doi.org/10.1016/j.precamres.2015.04.015

Vermeesch, P. (2018). IsoplotR: A free and open toolbox for geochronology. *Geoscience Frontiers*, *9*(5), 1479–1493. https://doi.org/10.1016/j.gsf.2018.04.001

Vielzeuf, D., Clemens, J. D., Pin, C., & Moinet, E. (1990). Granites, Granulites, and Crustal Differentiation. In *Granulites and crustal evolution* (Vol. 311). Springer. https://doi.org/10.1007/978-94-009-2055-2_5

Walsh, A. K., Kelsey, D. E., Kirkland, C. L., Hand, M., Smithies, R. H., Clark, C., & Howard, H. M. (2015). P–T–t evolution of a large, long-lived, ultrahigh-temperature Grenvillian belt in Central Australia. *Gondwana Research*, *28*(2), 531–564. https://doi.org/10.1016/j.gr.2014.05.012

Weinberg, R. F., & Hasalová, P. (2015). Water-fluxed melting of the continental crust: A review. *Lithos*, *212-215*, 158–188. https://doi.org/10.1016/j.lithos.2014.08.021

Wheller, C. J., & Powell, R. (2014). A new thermodynamic model for sapphirine: Calculated phase equilibria in K2O−FeO−MgO−Al2O3−SiO2−H2O−TiO2−Fe2O3. *Journal of Metamorphic Geology*, *32*(3), 287–299. https://doi.org/10.1111/jmg.12067

White, R. W., & Powell, R. (2002). Melt loss and the preservation of granulite facies assemblages. *Journal of Metamorphic Geology*, *20*(7), 621–632. https://doi.org/10.1046/j.1525-1314.2002.00206_20_7.x

White, R. W., Powell, R., & Clarke, G. L. (2002). The interpretation of reaction textures in Fe-rich metapelitic granulites of the Musgrave block, Central Australia: Constraints from mineral equilibria calculations in the system K2O–FeO–MgO–Al2O3–SiO2–H2O–TiO2–Fe2O3. *Journal of Metamorphic Geology*, *20*(1), 41–55. https://doi.org/10.1046/j.0263-4929.2001.00349.x

White, R. W., Powell, R., & Holland, T. J. (2007). Progress relating to calculation of partial melting equilibria for metapelites. *Journal of Metamorphic Geology*, *25*(5), 511–527. https://doi.org/10.1111/j.1525-1314.2007.00711.x

White, R. W., Powell, R., Holland, T. J., Johnson, T. E., & Green, E. C. R. (2014). New mineral activity-composition relations for thermodynamic calculations in metapelitic systems. *Journal of Metamorphic Geology*, *32*(3), 261–286. https://doi.org/10.1111/jmg.12071

White, R. W., Powell, R., Holland, T. J., & Worley, B. A. (2000). The effect of TiO2 and Fe2O3 on metapelitic assemblages at greenschist and amphibolite facies conditions: Mineral equilibria calculations in the system K2O–FeO–MgO–Al2O3–SiO2–H2O–TiO2–Fe2O3. *Journal of Metamorphic Geology*, *18*(5), 497–511. https://doi.org/10.1046/j.1525-1314.2000.00269.x

Whitehouse, M., & Platt, J. P. (2003). Dating high-grade metamorphism—Constraints from rare-earth elements in zircon and garnet. *Contributions to Mineralogy and Petrology*, *145*, 61–74. https://doi.org/10.1007/s00410-002-0432-z

Wiedenbeck, M., Alle, P., Corfu, F., Griffin, W. L., Meier, M., Oberli, F., Von Quadt, J. C., & Spiegel, W. (1995). Three natural zircon standards for U–Th–Pb, Lu–Hf, trace element and REE analyses. *Geostandards Newsletter*, *19*(1), 1–23. https://doi.org/10.1111/j.1751-908X.1995.tb00147.x

Wong, B. L., Morrissey, L. J., Hand, M., Fields, C. E., & Kelsey, D. E. (2015). Grenvillian-aged reworking of late Paleoproterozoic crust of the southern north Australian craton, Central Australia: Implications forthe assembly of Mesoproterozoic Australia. *Precambrian Research*, *270*, 100–123. https://doi.org/10.1016/j.precamres.2015.09.001

Xiang, H., & Connolly, J. A. D. (2021). GeoPS: An interactive visual computing tool for thermodynamic modelling of phase equilibria. *Journal of Metamorphic Geology*, *40*(2), 243–255. https://doi.org/10.1111/jmg.12626

Xu, H., Lei, H., Xiong, Z., & Zhang, J. (2019). Paleoproterozoic ultrahigh-temperature granulite-facies metamorphism in the Sulu orogen, eastern China: Evidence from zircon and monazite in the pelitic granulite. *Precambrian Research*, *333*, 105430. https://doi.org/10.1016/j.precamres.2019.105430

Yakymchuk, C., & Brown, M. (2014). Behaviour of zircon and monazite during crustal melting. *Journal of the Geological Society, London*, *171*, 465–479. https://doi.org/10.1144/jgs2013-115

Yakymchuk, C., Clark, C., & White, R. W. (2017). Phase relations, reaction sequences and Petrochronology. *Reviews in Mineralogy and Geochemistry*, *83*(1), 13–53. https://doi.org/10.2138/rmg.2017.83.2

Yakymchuk, C., Kirkland, C. L., & Clark, C. (2018). Th/U ratios in metamorphic zircon. *Journal of Metamorphic Geology*, *36*(6), 715–737. https://doi.org/10.1111/jmg.12307

Yang, P., & Pattison, D. (2006). Genesis of monazite and Y-zoning in garnet from the Black Hills, South Dakota. *Lithos*, *88*, 233–253. https://doi.org/10.1016/j.lithos.2005.08.012

Young, D. N., Fanning, C. M., Shaw, R. D., Edgoose, C. J., Blake, D. H., Page, R. W., & Camacho, A. (1995). U-Pb zircon dating of tectonomagmatic events in the northern Arunta inlier, Central Australia. *Precambrian Research*, *71*, 45–68. https://doi.org/10.1016/0301-9268(94)00055-V

Zeck, H. P., & Whitehouse, M. (2002). Repeated age resetting in zircons from Hercynian–Alpine polymetamorphic schists (Betic–Rif tectonic belt, S. Spain)—A U–Th–Pb ion microprobe study. *Chemical Geology*, *182*(2–4), 275–292. https://doi.org/10.1016/S0009-2541(01)00296-0

SUPPORTING INFORMATION

Additional supporting information can be found online in the Supporting Information section at the end of this article.

Appendix A. P/T-X models.
Appendix B. Micro zircon and monazite.
Appendix C. Orthopyroxene EPMA traverses and measured Al_2O_3 contents. (a) Measured Al_2O_3 content in wt% for sample 830–6, (b) spot locations on orthopyroxene for sample 830–6, (c) measured Al_2O_3 content in wt% for sample 830–7, (d) spot locations on orthopyroxene for sample 830–7.
Appendix D. Monazite spiderplots.
Appendix E. Titanite spiderplot.
Appendix F. Zircon spiderplots.
Table S1. Geochemistry.
Table S2. Zr-in-rutile temperatures for sample 830–20.
Table S3. Monazite U–Pb and TE.
Table S4. Zircon U–Pb and TE.
Table S5. Titanite U–Pb and TE.
Table S6. Garnet TE.
Table S7. Garnet Lu-Hf.

How to cite this article: March, S., Hand, M., Morrissey, L., & Kelsey, D. (2024). The inhibited response of accessory minerals during high-temperature reworking. *Journal of Metamorphic Geology*, *42*(2), 257–289. https://doi.org/10.1111/jmg.12754